INVESTIGATION OF CORIUM MELT INTERACTION WITH NPP REACTOR VESSEL STEEL (METCOR)

Phase 2

PROGRESS REPORT

01/01/05 – 31/03/05

Molten corium hydrodynamics and heat transfer under IMCC

Authors

Dr.(Eng.), Prof.	V. B. Khabensky
Ph.D.	S.A. Smirnov
Dr.(Eng.)	S. V. Bechta
Ph.D.	V. S. Granovsky
	S. A. Vitol
	E. V. Krushinov
Prof., Associate member of the Russian Academy of Sciences	V. V. Gusarov
Dr.(Eng.), Prof.	Yu. B. Petrov
Ph.D.	I. V. Kulagin
Ph.D.	D. B. Lopukh
Ph.D.	A. Yu. Pechenkov
Ph.D.	S. Yu. Kotova
Ph.D.	I. V. Poznyak
	V. I. Almjashev
	E. M. Belyaeva
	V. G. Bliznyuk
	V. R. Bulygin
	E. K. Kalyago
	N. E. Kamensky
	A. V. Lysenko
	A. P. Martynov
	V. V. Martynov
	E. V. Shevchenko
	A. A. Chertkov

ABSTRACT

The report presents the results of testing physicomathematical models that describe thermal hydraulics of the prototypic corium using experimental data from MC4 and MC5 tests performed on the Rasplav-2 and Rasplav-3 test facilities.

Numerical modeling made it possible to determine structure of the 2D and 3D nonstationary flow of molten corium in the cold crucible, as well as the heat fluxes from the surfaces bounding the molten pool. The calculations used both direct modeling of turbulence of the free convective current, and the k-ω turbulence model.

CONTENTS

Introduction

Prediction of thermal loads on the water-cooled walls (confining structures) is of special importance for retaining corium either in the nuclear reactor vessel or in an external catcher of the crucible type. Under the quasistable conditions, heat flux density distribution at the molten pool boundaries is determined by regularities of the free-convective heat transfer, which depends on intensity and distribution of heat sources, as well as on the molten pool dimensions and conditions at its boundaries. As a rule, the movement of the melt under the actual conditions is turbulent.

A series of software tools, including special-purpose ones, have been designed for applying to the above-mentioned conditions in order to model free-convective heat transfer. These tools have been verified to this or that extent, using tests with model liquids mostly, as up to now the majority of thermophysical properties of molten coriums and the type of boundary conditions in the solid-liquid area near the pool walls remain uncertain. These circumstances make the tests with prototypic corium especially valuable and offer better possibilities for the software tools verification. Experimental investigations of this very type are carried out in the framework of METCOR Project.

The present work was aimed at preparing the available software tools for the numerical support to and analysis of results from the METCOR tests, improvement and verification of these tools using the obtained experimental data. The analysis was applied to the MC4 and MC5 tests.

1. Physicomathematical model

1.1. Equations of motion, energy, continuity, and turbulence

The 3D nonstationary motion and heat transfer in a molten pool are described by the equations of Navier-Stokes, continuity and energy [1].

In the Boussinesq approximation (taking buoyancy into account), the Navier-Stokes equation is written as [1]:

$$c\frac{\partial\vec{V}}{\partial t}+c(\vec{V}\cdot\nabla)\vec{V}=-\mathrm{grad}\left(p+\frac{2}{3}\mu(T)\cdot\mathrm{div}\vec{V}\right)+\mathrm{Div}\left[\mu(T)\cdot\hat{S}\right]+c_{0\beta}(T-T_0)\vec{g}+\vec{F}(x,y,z), \qquad (1)$$

$$\mathrm{Div}(\hat{S})=\frac{\partial S_{ji}}{\partial x_i}, \qquad (2)$$

$$\hat{S}=\begin{bmatrix}\frac{\partial u}{\partial x}, & \frac{1}{2}\left(\frac{\partial u}{\partial y}+\frac{\partial v}{\partial x}\right), & \frac{1}{2}\left(\frac{\partial u}{\partial z}+\frac{\partial w}{\partial x}\right)\\ \frac{1}{2}\left(\frac{\partial v}{\partial x}+\frac{\partial u}{\partial y}\right), & \frac{\partial v}{\partial y}, & \frac{1}{2}\left(\frac{\partial v}{\partial z}+\frac{\partial w}{\partial y}\right)\\ \frac{1}{2}\left(\frac{\partial w}{\partial x}+\frac{\partial u}{\partial z}\right), & \frac{1}{2}\left(\frac{\partial w}{\partial y}+\frac{\partial v}{\partial z}\right), & \frac{\partial w}{\partial z}\end{bmatrix}, \qquad (3)$$

where t is time; x, y, z are Cartesian coordinates; T, $\vec{V}$, ρ, p is temperature, velocity vector, density, and pressure; β is the coefficient of volumetric expansion; ρ_0 is density at a temperature T_0; μ is the coefficient of dynamic viscosity; $\vec{g}$ is the gravitational acceleration; $\vec{F}$ is the bulk force of non-gravitational origin; $\hat{S}$ is the strain rate tensor; u, v, w are the components of the velocity vector $\vec{V}$ along x, y, z coordinates.

Equation (1), supplemented by the continuity equation:

$$\mathrm{div}\vec{V}=0, \qquad (4)$$

describes motion of an isothermal liquid. For a non-isothermal liquid in the case with the present melt, a closure of (1)÷(4) is required by the energy equation [1]:

$$cc\frac{\partial T}{\partial t}+cc(\vec{V}\cdot\nabla)T=\mathrm{div}\left[\lambda(T)\cdot\mathrm{grad}T\right]+W(x,y,z), \qquad (5)$$

where c is heat capacity; λ is thermal conductivity; W is the power of volume heat release.

The gravitational force $c_{0\beta}(T-T_0)\vec{g}$ in equation (1) causes free-convective flow when the temperature gradient is directed along vector $\vec{g}$ and the condition $d\rho/dT<0$ is fulfilled.

$\vec{F}$ force in equation (1) and the volume heat source W in equation (5) possess electromagnetic nature under the conditions of METCOR tests; their distribution in the melt is given in Section 1.3, and the calculation method is described in [2, 3].

The molten pool geometry in MC4 and MC5 is close to cylindrical, with a vertical symmetry

axis, and that is why in addition to the 3D model based on equations (1)÷(5) the present work considers a 2D axis symmetrical model in which the Navier-Stokes equation is written as:

$$c\frac{\partial u}{\partial t}+cu\frac{\partial u}{\partial r}+cv\frac{\partial u}{\partial z}=-\frac{\partial p}{\partial r}+\frac{1}{r}\frac{\partial}{\partial r}\left(м(T)\cdot r\frac{\partial u}{\partial r}\right)-м(T)\frac{u}{r^2}+\frac{\partial}{\partial z}\left(м(T)\cdot r\frac{\partial u}{\partial z}\right)+F_r\ , \quad (6)$$

$$c\frac{\partial w}{\partial t}+cu\frac{\partial v}{\partial r}+cv\frac{\partial v}{\partial z}=-\frac{\partial p}{\partial z}+\frac{1}{r}\frac{\partial}{\partial r}\left(м(T)\cdot r\frac{\partial v}{\partial r}\right)+\frac{\partial}{\partial z}\left(м(T)\cdot r\frac{\partial v}{\partial z}\right)- \quad (7)$$

$$-c_0в(T-T_0)g+F_v\ ,$$

$$\frac{\partial u}{\partial r}+\frac{u}{r}+\frac{\partial v}{\partial z}=0\ . \quad (8)$$

Energy equation:

$$cc\frac{\partial T}{\partial t}+cc\ \ u\frac{\partial T}{\partial r}+cc\ \ v\frac{\partial T}{\partial z}=\frac{1}{r}\frac{\partial}{\partial r}\left(л(T)\cdot r\frac{\partial T}{\partial r}\right)+\frac{\partial^2 T}{\partial z^2}+W(r,z)\ , \quad (9)$$

where r is the radius; z is the height; u, v are the radial and vertical components of velocity; F_r, F_v are the bulk force radial and vertical components. Other parameters are designated as in (1).

Equations (1)÷(5) describe both laminar and turbulent 3D flows. The same refers to the 2D equations (6)÷(9) with an only reservation that turbulence has a 3D nature, and its 2D description is a rough approximation, applicability of which to the given conditions is checked by experimental data, or by the results of verified 3D calculations.

Analytical methods of solving the Navier-Stokes equation have been developed for a narrow circle of tasks and are inefficient in the present case. Therefore, calculations of the melt motion in the cold crucible require application of numerical methods which allow calculation of both laminar and turbulent flows.

The dimensionless similarity criterion, which is usually used in the engineering practice for evaluating flow condition near a heated body, is the Rayleigh number:

$$Ra=\frac{вgc_*^2c(T_s-T_\infty)L^3}{м_*л_*}\ , \quad (10)$$

Here T_s, T_∞ are the maximum body temperature, and the minimum temperature in the surrounding liquid far zone; ρ_*, μ_*, λ_* are density, dynamic viscosity and thermal conductivity at $T_* = 0.5\cdot(T_s+T_\infty)$; L is the characteristic dimension of the system.

The Rayleigh number (10) equals the Grashof number (Gr) by the Prandtl number: Ra=Gr·Pr.

The Prandtl number characterizes similarity of temperature and dynamic parameters of a flow:

$$\mathrm{Pr} = \frac{\text{см}_*}{\text{л}_*} \ , \qquad (11),$$

while the Grashof number is determined by the relation of the lifting force $\text{с}_0\text{в}g(T_s - T_\infty)L$ to the internal friction force (per unit area) мV/L, where V is the velocity scale, which for the free-convective flow may be given as м/cL,

$$\mathrm{Gr} = \frac{\text{в}g\text{с}_*^2(T_s - T_\infty)L^3}{\text{м}_*^2} \ , \qquad (12)$$

Thus, the Grashof number is determined by relations between dynamic parameters only, while the Rayleigh number additionally includes the criterion of similarity of velocity and temperature characteristics (the latter also influence intensity of free convection). For example, when thermal conductivity of a liquid increases, thickness of the boundary layer near the heated body surface decreases, which means shrinking of a zone with nonequilibrium stratification and, consequently, a drop in the free convection intensity (the Rayleigh number decreases at that).

According to [4], for an isothermally heated cylinder or a vertical plate free convection changes from laminar to turbulent within the $10^7<\mathrm{Ra}<10^9$ range. However, the criteria revealed in the ordinary hydrodynamic tests may be used for analyzing METCOR tests only approximately, as under the METCOR conditions heat release in the melt is non-uniform in the volume, and in some cases the role of Lorentz forces is significant. Besides, for a melt heated up to about 3000 K the role of radiation from the free surface is noticeable, and it is not taken into account in (10).

Conditions of MC4 are similar to [4], because release of electromagnetic power occurs in MC4 near the walls, while influence of the electromagnetic force is not big, if compared with the gravitational. As the Rayleigh number in MC4 is about $3\cdot10^9$ and this value corresponds to the transition to the turbulent flow [4], it may be supposed that the melt motion in MC4 is rather turbulent than laminar. Observations of the melt corroborate this supposition. A similar conclusion can be made for MC5.

The tasks concerning internal heat release also employ the modified Rayleigh number, $\mathrm{Ra}^*=\mathrm{Ra}\cdot\mathrm{Da}$, where Da is the Damkohler number:

$$\mathrm{Da} = \frac{q_v L^2}{\text{л}_*(T_s - T_\infty)} \qquad (13)$$

Here, q_v is the volume heat source. From (10) and (13) it follows that

$$\mathrm{Ra}^* = \frac{\text{в}g\text{с}\text{с}_*^2 q_v L^5}{\text{м}_*\text{л}_*^2} \qquad (14)$$

Turbulence starts showing at $\mathrm{Ra}^*>10^{10}$, and for both MC4 and MC5 this condition is

observed, as $2\cdot10^{10}<Ra^*<5\cdot10^{10}$ under conditions of the ingots. Therefore, the models under development should describe turbulent motion of the melt.

Specific conditions of the METCOR tests complicate selection of an adequate model of turbulence based on the RANS method (RANS – Raynolds-averaged Navier-Stokes). For instance, the well-known k-ε model contains adjustable parameters, numerical values of which have been determined for a relatively narrow circle of conditions.

A search for, or development of a new RANS-class model of turbulence may be avoided thanks to direct numerical modeling of turbulence using the nonstationary equations of Navier-Stokes. Such an approach requires the linear dimension of the computation cell to be below the Kolmogorov scale of turbulence, which characterizes the minimal size of the turbulent vortex.

The Kolmogorov scale may be appreciated using the formula [5]:

$$\text{з} = \left(\frac{\text{н}^3}{\text{е}} \right)^{\frac{1}{4}}, \tag{15}$$

where ν is the kinematic viscosity coefficient; ε is the turbulent energy dissipation rate. It will be shown below (Section 3.1) that the value of η under the conditions of MC4 is within the 0.17÷0.55 mm range, while in the greater part of the melt η is about 0.35 mm. This basically makes it possible to perform direct calculaations of a 2D or 3D turbulent flow of the melt in the cold crucible of Rasplav-2 and Rasplav-3 test facilities using a PC.

Obviously, an advantage of direct modeling of turbulence is in obtaining local pulsation characteristics of the flow and of information about its spatial structure, but since calculaations of the nonstationary flow may require more time than required for calculating the stationary flow, it may be expedient to determine the possibility of computing a turbulent melt using the RANS models. In the RANS method, the Navier-Stokes equations are written as (1), (5) with the only difference that viscosity and thermal conductivity are substituted by effective coefficients:

$$\text{м}_{\text{eff}} = \text{м} + \text{м}_{\text{t}}, \tag{16}$$

$$\text{л}_{\text{eff}} = \text{л} + \text{л}_{\text{t}}, \tag{17}$$

Here, μ_{eff}, λ_{eff} are coefficients of effective dynamic viscosity and effective thermal conductivity; μ_t, λ_t are coefficients of turbulent viscosity and turbulent thermal conductivity.

The present work employs the k-ω turbulence model, in which the kinematic coefficient of turbulent viscosity ν_t is determined by the formula

$$\text{н}_{\text{t}} = \text{С}_{\text{м}} \frac{\text{k}}{\text{щ}}, \quad \text{е} = \text{щk}, \tag{18}$$

where k is the turbulent kinetic energy; ω is the turbulent energy specific dissipation rate; ε is the turbulent energy dissipation rate; $C_м$ is a constant. The turbulent Prandtl number for

determining turbulent thermal conductivity was believed to be $Pr_t = 0.9$ ($Pr_t = c\mu_t/\lambda_t$, $\mu_t = \rho\nu_t$). The k-ω turbulence model has been chosen because it seems to be more accurate [6] in describing transfer coefficients for the spatially complex convective flow than the standard k-ε turbulence model.

According to the k-ω model [7], equations of turbulent kinetic energy transfer and of its dissipation rate are as follows:

$$\frac{\partial(ck)}{\partial t} + (\vec{V}\cdot\nabla)(ck) = Pc - c_{щ}k + \nabla\left[\left(м + \frac{м_t}{y_k}\right)\nabla k\right], \tag{19}$$

$$\frac{\partial(c_{щ})}{\partial t} + (\vec{V}\cdot\nabla)(c_{щ}) = C_{щ_1}\frac{cP_{щ}}{k} - C_{щ_2}c_{щ}^2 + \nabla\left[\left(м + \frac{м_t}{y_{щ}}\right)\nabla щ\right], \tag{20}$$

$$P = \frac{2}{3}k\,\mathrm{div}\,\overline{V} - н_t\left\{2\left[\left(\frac{\partial u}{\partial x}\right)^2 + \left(\frac{\partial v}{\partial y}\right)^2 + \left(\frac{\partial w}{\partial z}\right)^2\right] + \left(\frac{\partial u}{\partial x} + \frac{\partial v}{\partial y} + \frac{\partial w}{\partial z}\right)^2 - \frac{2}{3}\left(\mathrm{div}\,\overline{V}\right)^2\right\}, \tag{21}$$

where P is the source of the turbulent kinetic energy; $C_{щ_2} = 0.833$; $C_м = 0.09$; $C_{щ_1} = 0.555$; $y_k = y_{щ} = 2.0$.

It was stated above that the realization of RANS may be associated with problems concerning determination of an adequate model of turbulence. On the other hand, a decrease of the computational cell scale and hence, increase of the computational domain will make direct modeling of turbulence on a PC very labour-consuming due to a large number of cells in the computational grid. In such a case, the optimal solution would be to apply the LES (Large Eddy Simulation) method, which uses numerical analogs of the Navier-Stokes equations (1)÷(9) for solving problems concerning large vortex structures with a spatial scale exceeding linear size of a computational cell, and special algorithms – for determining local parameters of turbulence within each computational cell. This is an efficient method, as statistical characteristics of a smaller-area turbulence may be predicted better than those of a large-scale vortex structure. The LES method is not used in the present work for melt modeling, though its application is planned for the next stage.

Thus, the present investigation included a direct numerical modeling of a turbulent flow under the conditions of MC4 and MC5 tests, using nonstationary 3D and 2D Navier-Stokes equations (1)÷(9). Also, the k-ω turbulence model was used for the 2D flow calcultions.

The discrete analogs of differential equations have been constructed using the finite volumes method [8] using the rectangular mesh. Calculation of the velocity and pressure fields was done using the semi-implicit SIMPLE (Semi-Implicit Method for Pressure-Linked Equations) method. The solution algorithm is realized in the DYMELT code.

1.2. Heat transfer properties of the melt

At present, molten corium properties are known approximately; their significant part is accumulated in the MATRO library. When determining some heat transfer parameters we used data from the said library, as well as from the works [2, 9, 10]. These sources contain the most complete database for MC5 and a bit less comprehensive one for MC4. The missing parameters for MC4 were taken as analogs or from quantitative assessments.

MC4 test:

- Corium composition – 56.1% UO_2 + 23.9%ZrO_2 + 20.0%FeO
- Heat capacity – c = 540 J/kg
- Density at 2700 K – ρ_0 = 7500 kg/m^3
- Volumetric expansion coefficient – $\beta = 1.4 \cdot 10^{-4}$ K^{-1}
- Thermal conductivity – λ = 2 W/m·K
- Emissivity factor – ε = 0.8
- Liquidus temperature – T_L = 1910 °C, [2]
- Solidus temperature – T_S = 1400 °C (thermodynamic evaluation)
- Fusion heat – $3 \cdot 10^5$ J/kg
- Dynamic viscosity coefficient was calculated using formula [9]:

$$m = m_0 \left(1 + \frac{0.75 \, fvs / fvs\max}{1 - fvs / fvs\max} \right)^2 , \qquad (22)$$

where f_{vs} – volume fraction of the solid phase which changes from 1 to 0 at the melt temperature shift from T_S to T_L; f_{vsmax} = 0.635. We assumed μ_0 to be equal to 0.0065 Pa·s;

It is seen from (22) that $\mu \to \infty$ is effective at $f_{vs} \to f_{vsmax}$. At $f_{vs} \geq f_{vsmax}$, we assumed μ = 100 Pa·s in the calculations. As the result, corium crust modeling became possible, because melt motion stopped in the zone with μ = 100 Pa·s due to strong friction. The mentioned procedure is of importance for performing the coordinated calculation, as preliminary determination of the melt crust boundaries, which is nonstationary under some regimes, becomes unnecessary.

MC-5 test:

- Corium – C-100
- Liquidus/solidus temperature – $T_{L/S}$ =2550 °C
- Heat capacity – c = 540 J/kg
- Density at 2700 K – ρ_0 = 7400 kg/m^3
- Volumetric expansion coefficient – $\beta = 0.61 \cdot 10^{-4}$ K^{-1}
- Emissivity factor – ε = 0.8

- Fusion heat – $3.2 \cdot 10^5$ J/kg
- Tab. 1 contains data on thermal conductivity vs. temperature according to [10] at $T<T_{L/S}$.

Table 1. Thermal conductivity vs. temperature

T, K	300	1000	1500	2000	3000
λ, W/(m·K)	7.7	3.01	2.15	2.00	2.8

At $T>T_{L/S}$ thermal conductivity λ is assumed to be equal 2.8 W/(m·K), which agrees with [10].

- The kinematic viscosity coefficient at $T > T_{L/S}$ is given in Tab. 2, [10].

Table 2. Kinematic viscosity coefficient vs. temperature

T, ^{o}C	2600	2650	2700	2750	2800
$\nu \cdot 10^7$, m^2/s	9.49	8.83	7.37	7.66	6.83

For calculating the melt crust at $T<T_{L/S}$, as well as for the MC4 regime, viscosity was assumed as μ = 100 Pa·s, or $\nu = 1.33 \cdot 10^{-2}$ m^2/s.

1.3. Computational domain geometry in MC4, MC5. Electromagnetic sources of heat and forces.

Power in the melt from induction heating and Lorentz forces are calculated separately from thermal hydrodynamics [2, 3] by means of software tools developed by the Department of Electrotechnological and Converter Equipment at the St.Petersburg Electrotechnical University (SPbGETU). A combined method of electromagnetic calculation has been applied, in which the exterior problem was solved using integral equations, while the inner problem (in the melt) was solved by means of the finite elements method. The obtained data on energy release and Lorentz forces served as the input data for calculating heat-and-mass transfer.

Figs. 1, 2 offer induction furnace schematics in MC4 and MC5. In the framework of the present investigation, their main difference is in the elements that form the molten pool bottom. In MC4 it is a water-cooled three-section calorimeter and in MC5 it is the steel specimen upper surface. In both cases the crucible consists of 20 water-cooled copper tubes Ø 10 mm each. Diameter of the circle inscribed in the crucible horizontal section is 71 mm. In MC4, diameter of the bottom calorimeter central section was 30.5 mm, while inner and outer diameters of the middle section were 30.5 and 51.5 mm, respectively.

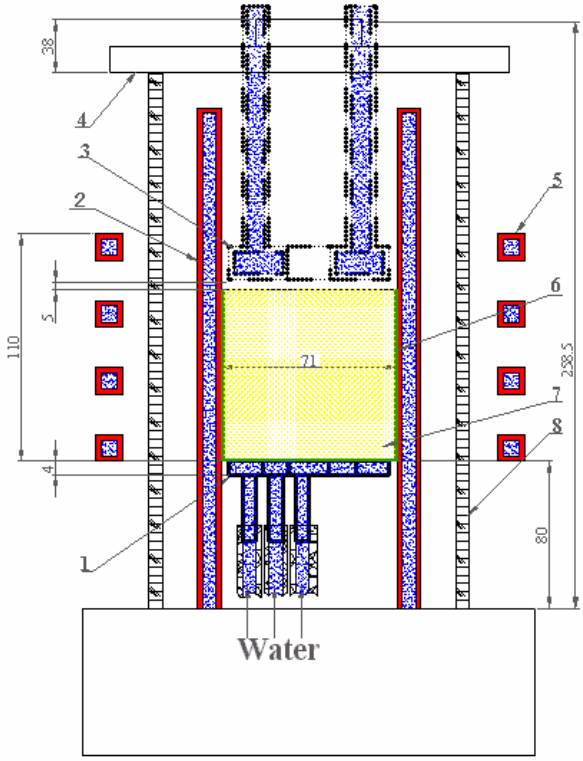

1.- bottom calorimeter; 2 – cold crucible; 3 – top quartz calorimeter; 4 – cover; 5 – inductor; 6 – crust; 7 – molten corium; 8 – quartz tube

Fig. 1. Furnace schematics in MC4.

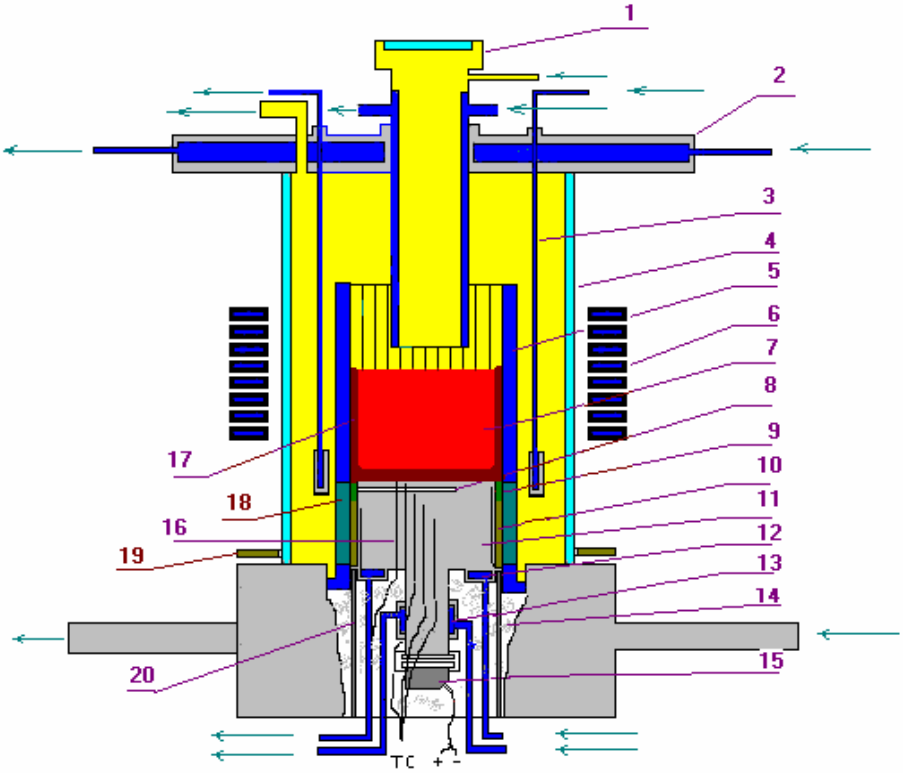

1 – water-cooled pyrometer shaft; 2 – water-cooled cover; 3 – water-cooled electromagnetic screen; 4- quartz tube; 5 – crucible section; 6 – inductor; 7 – melt; 8 – acoustic defect; 9 – fused ZrO_2 (fianite); 10 – ZrO_2 powder; 11 – vessel steel specimen; 12 – top specimen calorimeter; 13 – bottom specimen calorimeter; 14 – mullite wool insulation; 15 – ultrasonic sensor; 16 – K-type thermocouples; 17 – skull, 18 – electromagnetic screen (crucible sections are welded together); 19 – uncooled electromagnetic screen; 20 – cylindrical support of the specimen.

Fig. 2. Furnace schematics in MC5

The following experimental data were used for verifying the physicomathematical models:

MC4 test:

1. Temperature in the melt surface central zone, averaged for about a Ø 4 mm area;
2. Heat flux from the melt free surface;
3. Heat flux to the crucible;
4. Heat fluxes to the bottom calorimeter central and middle sections;
5. Crust thickness above the bottom calorimeter center;
6. Video of the melt free surface central zone Ø 21 mm.

MC5 test:

1. Temperature in the melt surface central zone, averaged for about a Ø 4 mm area;
2. Heat flux to the crucible;
3. Crust thickness above the specimen center;
4. Temperature distribution in the specimen
5. Video of the melt free surface central zone Ø 21 mm.

Figs 3 & 4 show the furnace and crucible from MC5, and Fig. 5 offers the molten pool diagram.

Fig. 3. Furnace after MC5

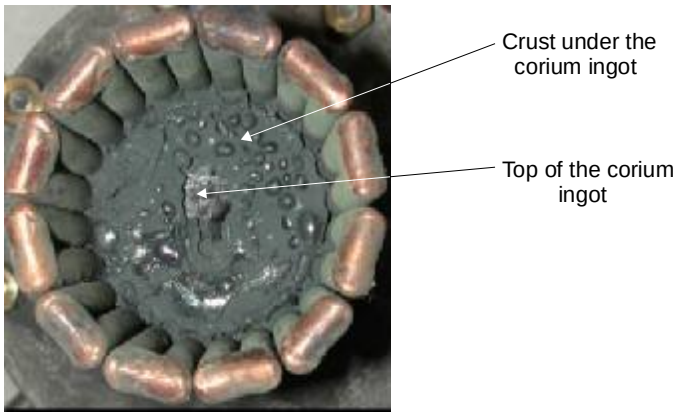

Fig. 4. Corium ingot in the cold crucible in MC5

The space near the crucible walls is evidently 3D and lacks axial symmetry, but since the size of tubes is much smaller than the molten pool diameter, a geometry simplified to a Ø 71 mm cylinder (Fig. 6) was used for calculations.

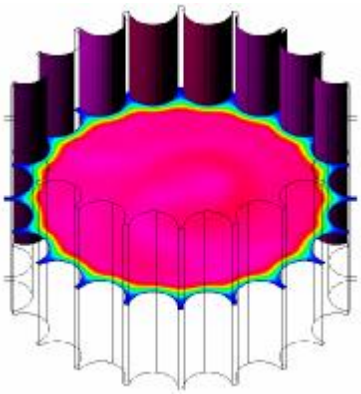

Fig.5. Diagram of the molten pool in the cold crucible

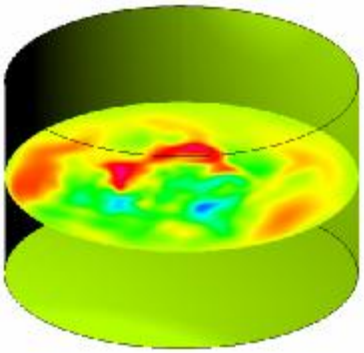

Fig.6. Molten pool geometry for calculations

Besides, cylindrical geometry has been chosen for hydrodynamic calculations because electromagnetic sources of heat and Lorentz forces have been calculated especially for it [2, 3]. When setting the temperature boundary condition for the lateral crust in the simplified geometry (Fig. 6) it was taken into account that the internal surface area of a real crucible 1.45 times exceeds the lateral surface area of a cylinder inscribed into the crucible.

Figs. 7 ÷ 12 show distribution of volume heat sources and forces [2, 3]. It can be seen that though the volume heat sources are intercomparable, electromagnetic forces in MC5 are by an order of magnitude stronger than in MC4. In both cases, the radial component of the force is directed towards the axis, and the axial component – downwards.

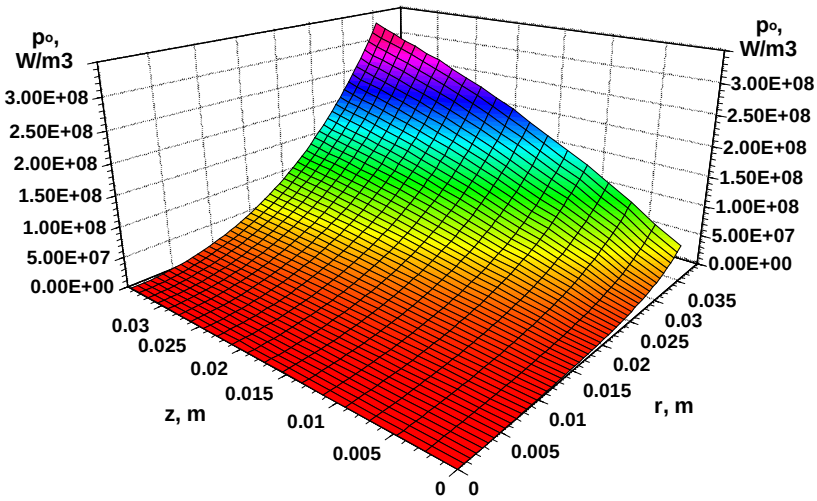

Fig. 7. Distribution of volume heat sources in MC4, regime #1

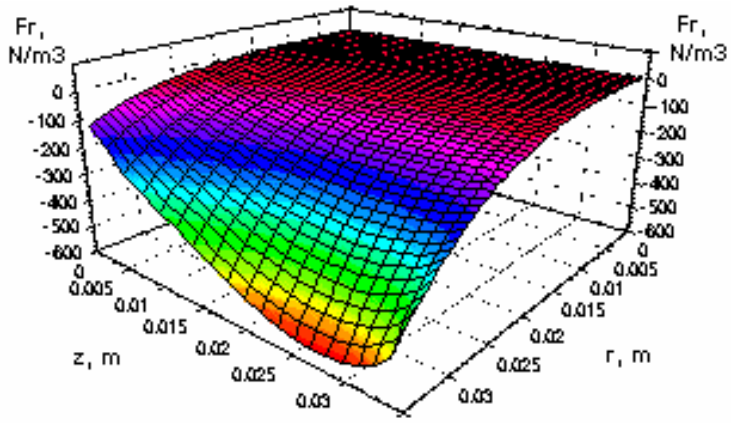

Fig. 8. Distribution of the radial bulk force in MC4, regime #1

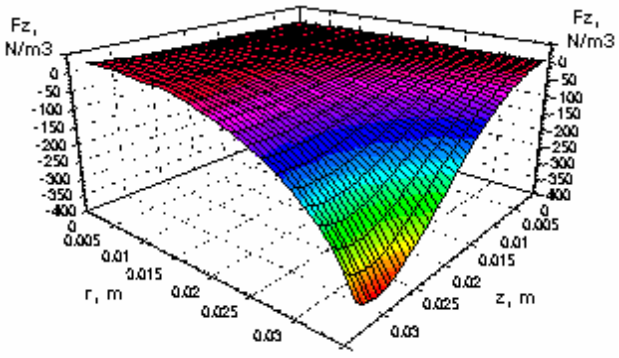

Fig. 9. Distribution of the axial bulk force in MC4, regime #1

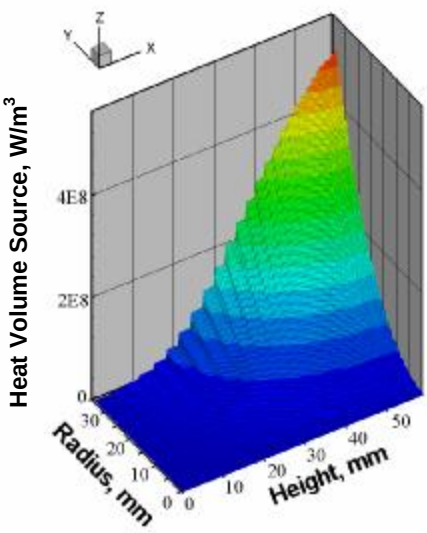

Fig. 10. Distribution of volume heat sources in MC5, regime #1

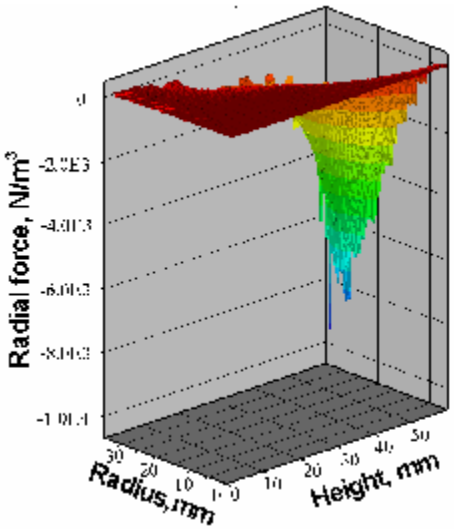

Fig. 11. Distribution of the radial bulk force MC5, regime #1

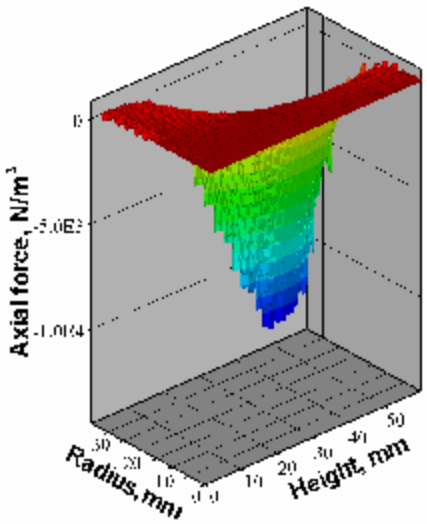

Fig. 12. Distribution of the axial bulk force in MC5, regime #1

1.4. Boundary conditions

Temperature. The choice of the boundary conditions type regarding temperature on the cold (water-cooled) walls of the structure, i.e., on the bottom calorimeter in MC4 and the crucible in both MC4 and MC5 was based on the provisions described below. The material of cold walls of the crucible and calorimeter does not chemically react with corium and therefore there are no factors to cause strong adhesion of the crust to the said metallic surfaces. Besides, the crust experiences nonuniform thermal stress and, hence, it is deformed. This, as well as the presence of powdered charge in the layer adjacent to the water-cooled surfaces, determines contact thermal resistance [11, 12], which leads to a big temperature gradient in the effective gap between the rough surface of the skull and metal (Fig. 13).

Through this gap, heat is transported by both radiation and thermal conductivity, therefore we use a boundary condition for the heat flux density:

$$л\frac{\partial T}{\partial n} = ey\left(T^4 - T_W^4\right) + б\left(T - T_W\right), \tag{23}$$

where T_w is the wall temperature, T is the temperature of the corium crust outer surface, n is the wall normal, α is the effective heat transfer coefficient.

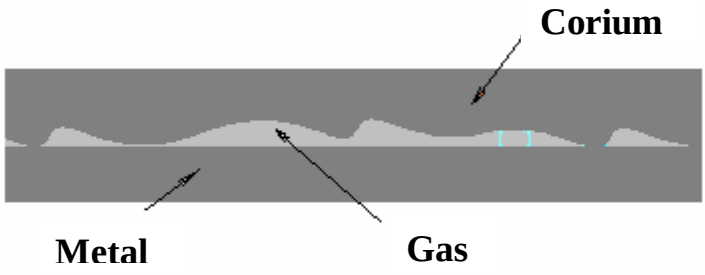

Fig. 13. Diagram of the corium crust/water-cooled metallic surface contact zone

In [6] there was noted the difficulty of determining boundary conditions at the corium crust outer surface in the crucible with cold walls, and a condition was proposed:

$$л_{eff}\frac{\partial T}{\partial n} = H(T)\cdot\left(T - T_W\right), \tag{24}$$

where H(T) is an empirical, temperature-dependent heat transfer coefficient. It was not specified in [6]. Our notions agree with [6], as the comparison of (23) with (24) yields:

$$H(T) = ey\left(T + T_W\right)\cdot\left(T^2 + T_W^2\right) + б \tag{25}$$

Condition (23) was analyzed during the calculations using different α values (Section 3.1.).

In MC5, in addition to the considered loose contact of the crust with cold metal, a tight bond between the high-temperature specimen surface and corium crust realized from their chemical reaction. For this boundary, the calculations used the condition of the conjugated heat exchange:

$$л_{Corium} \frac{\partial T_{Corium}}{\partial n_{Corium}} = л_{Metal} \frac{\partial T_{Metal}}{\partial n_{Metal}} \quad (26)$$

A boundary condition of the second kind was set at the melt free surface for density of the radiation-determined heat flux. Taking into account the fact that the melt free surface and the surrounding surfaces form a closed optical system, and temperature of the latter (thanks to cooling) is low, the boundary condition is written as

$$л_{eff} \frac{\partial T}{\partial n} = eyT^4, \quad (27)$$

where $\lambda_{eff} = \lambda + \lambda_t$ when the k-ω turbulence model is used, and $\lambda_{eff} = \lambda$ at direct modeling the flow using the full system of Navier-Stokes equations.

Dynamic characteristics. The condition of adhesion was set for the walls of the crucible, calorimeter and specimen. Under this condition, all components of corium velocity equal zero:

$$u = v = w = 0. \quad (28)$$

The condition of k = 0 was set for the turbulent kinetic energy at the walls. Another condition was specified for the rate of dissipation (ω) in centers of the computational grid boundary cells:

$$щ = 7.2 \frac{н}{y_c^2}, \quad (29)$$

where y_c is the distance along the wall normal from the computational cell center.

The velocity component, perpendicular to the surface, equals zero at the melt free surface. The derivatives of the longitudinal velocity with respect to the normal to the melt free surface, as well as of the k and ω values, also equal zero, i.e., the melt glides along the surface without resistance of the outer gas medium.

2. Test problem: flow in a cavern

The testing was aimed at determining the solution grid convergence and the average Nusselt number at the computational domain boundaries. A 2D problem concerning natural thermal convection in a horizontal channel with square cross-section was chosen [13], Fig. 14. The cavern horizontal walls are thermally insulated, while the vertical ones have permanent temperatures $T_1 > T_2$.

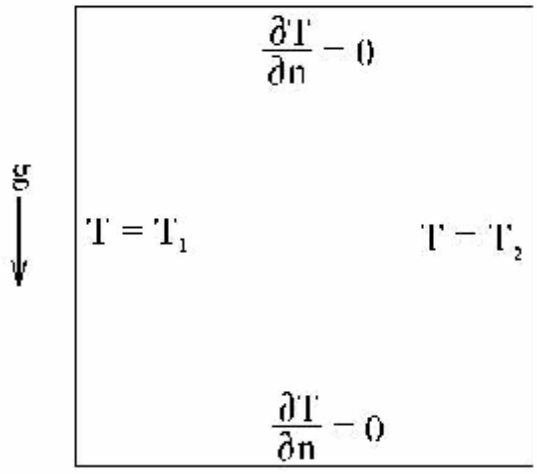

Fig. 14. Computational domain geometry and the wall boundary conditions for the test problem

The calculations have been performed for a gas with molar mass of 29 kg/Kmol, other parameters being:

- Rib length L = 0.045 m
- Pressure p = 106604 Pa
- Dynamic viscosity coefficient $\mu = 1.8 \cdot 10^{-5}$ Pa
- Thermal conductivity $\lambda = 2.55 \cdot 10^{-2}$ W/(m·K)
- Heat capacity $c_p = 1058$ J/(kg·K)
- Three regimes have been considered:

  (1) $T_1 = 300.5$ K, $T_2 = 299.5$ K, $Ra = 10^4$,

  (2) $T_1 = 305$ K, $T_2 = 295$ K, $Ra = 10^5$,

  (3) $T_1 = 350$ K, $T_2 = 250$ K, $Ra = 10^6$,

  The Rayleigh number is calculated by formula (30):

$$Ra = \frac{g c_*^2 c_p (T_1 - T_2) L^3}{T_{M_* Л_*}}, \qquad (30)$$

which is a modified (10) for the ideal gas at $T_S = T_1$, $T_\infty = T_2$, $T = 0.5 \cdot (T_1 + T_2)$.

Tab. 3 contains the Nusselt number average values for the cold wall, calculated by the formula

$$\langle Nu \rangle = \frac{1}{L} \int_0^L Nu(y) dy \quad , \qquad (31)$$

where

$$Nu(y) = \frac{L}{ДT} \frac{\partial T}{\partial n} \quad . \qquad (32)$$

Table 3. Nusselt number average values for the cold wall ($Ra = 10^5$)

	$\langle Nu \rangle$	
Cell number	Present work	Source [13]
40×40	4.5376	4.61653
80×80	4.5353	4.51945
160×160	4.5183	
320×320		4.52164

It can be seen that with the use of a 160×160 grid, the difference of our result from the grid-independent value [13] equals 0.07 %.

Tab. 4 compares the Nusselt numbers at different Rayleigh numbers. The former were obtained in the present work using a 160×160 grid and compared with the grid-independent values [13]. In [13], the grid-independent value was obtained using a 320×320 grid. The agreement between the results is satisfactory.

Table 4. Comparison of the Nusselt numbers at different Rayleigh numbers (160´160 grid)

	$\langle Nu \rangle$	
Ra	Present work	Source [13]
10^4	2.2380	2.2448
10^5	4.5183	4.52164
10^6	8.91204	8.8251

The temperature fields for Ra = 10^4 and Ra = 10^6 are shown in Fig. 15.Under both regimes the single-vortex laminar flow is realized, though at Ra = 10^6 a tendency towards formation of additional vortexes in the turning zones of the ascending and descending flows. These are the initial signs of the flow in transition regime.

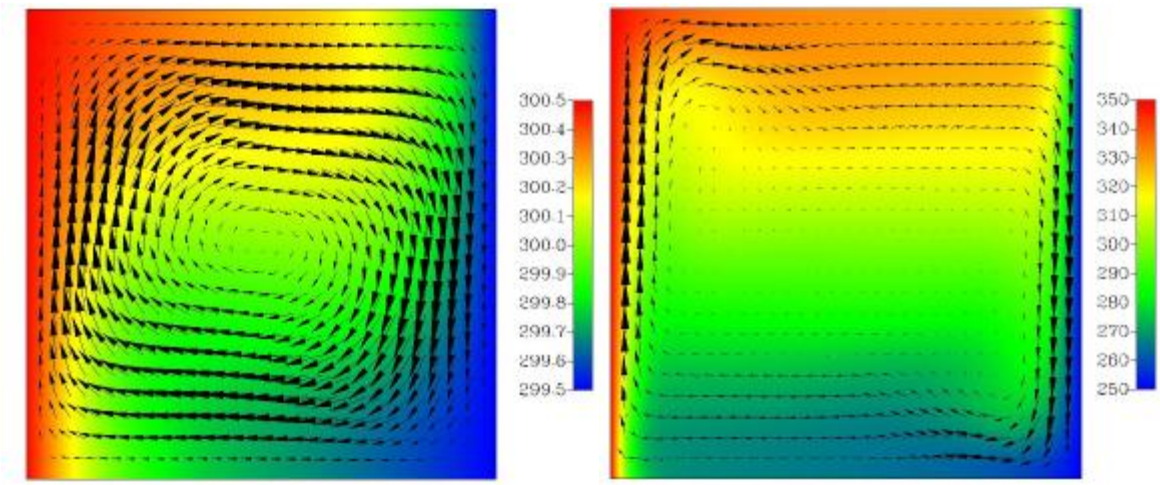

(a) (b)

Fig. 15. Velocity vectors and temperature distribution:
(a) – Ra = 10^4 , (b) – Ra = 10^6

3. Results of computations for MC4

3.1. Two-dimensional calculations

The four regimes of the MC4 test differed from one another by the molten pool depth and the power absorbed by the melt. Each regime was calculated with the use of both a 2D analog of the complete system of Navier-Stokes equations (6)÷(9) and additional inclusion of the k-ω turbulence model (19)÷(20) in the system (6)÷(9).

The computational domain diagram with a 35.5 mm radius is given in Fig. 16. The upper boundary corresponds to the melt free surface, the lateral – to the crucible, and the lower – to the bottom calorimeter sections. Tab. 5 contains data on height of the melt, power absorbed by the melt, and number of cells in the computational grid for regimes ## 1÷4. The rib of a computational cell is approximately 0.4 mm long. It was stated above that the power absorbed by the melt had been determined in advance by electromagnetic calculations [2, 3] based on experimental data concerning inductor voltage and heat fluxes from the melt and working chamber components to the calorimeters.

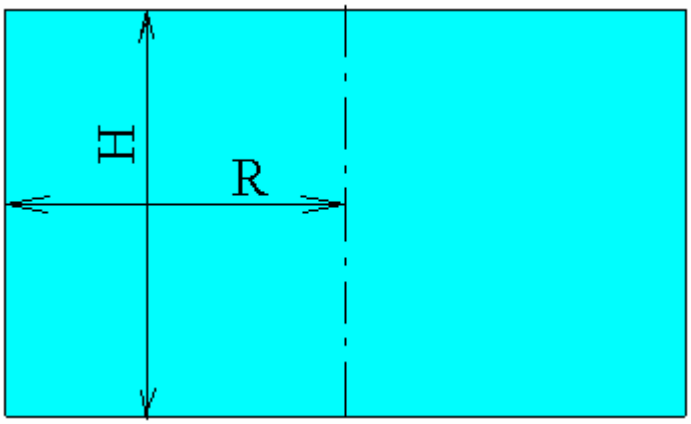

Fig. 16. Computational domain diagram

Table 5. Melt height; power absorbed by the melt; number of cells in the computational grid for regimes ## 1 ¸ 4

Regime	Melt height, mm	Power absorbed by the melt, W	Number of cells
1	42	16350	9856
2	42.5	30200	9856
3	81.5	32660	17600
4	79	25520	17600

The wall temperature boundary condition was written as (23) when effective heat transfer coefficients were α=0 and α=150 W/(m^2·K). Here, the value of α is an adjustable parameter, as the self-consistent problem of α determination was not solved. At this stage it was important to ascertain the possibility of finding a plausible value of α which would cause a below 30% mismatch between the calculated and experimental values for heat fluxes under all four regimes of the test.

At α = 0, the heat flux is determined by radiation only, and this approximation is just for the high-temperature boundaries of the crust. The α value of 150 W/(m^2·K) corresponds to the gaseous gap with thickness (h) of 1 mm and thermal conductivity λ=0.15 W/(m·K), i.e. a thickness comparable with a skull grain size and thermal conductivity by an order of magnitude lower than that of solid corium.

Experimental and calculated values of heat fluxes, temperatures and crust thickness for the regimes ##1÷4 are given in Tabs. 6÷9, and the mismatch of experimental and calculated data are given in percentage terms (also, the absolute deviation ΔT is given for the temperature). All the calculated parameters have been averaged for a 5 min interval after the establishment of a quasiequilibrium regime. The crust thickness was determined from the T = T_{sol} isotherm. The temperature of the melt free surface central spot (T_{ev}) was obtained by averaging the heat flux from S – a Ø 4 mm area, which corresponds to the pyrometer sighting spot:

$$T_{ev} = \left(\frac{1}{S} \int_S T^4 ds \right)^{0.25} . \qquad (30)$$

Table 6. Comparison of experimental and calculated values. Regime # 1

Parameter	Test	Calculated α=150	Calculated α=0	Calculated, k-ω turbulence model α=150
Power of radiation from the melt surface, W	5300	4645 **14%**	4645 **14%**	5073 **4.2%**
Temperature of the melt surface central spot	2025, C	1928, C **4.7%** **(DT=97 K)**	1921, C **5.1%** **(DT=104 K)**	2007, C **0.9%** **(DT=18 K)**
Crust thickness on the bottom calorimeter, mm	5.5	8.3 **50%**	3.9 **29%**	6.7 **21%**
Power from the melt to:				
- crucible, W	10200	11259.6 **10 %**	11211.7 **11 %**	10769 **5.5%**
- calorimeter central section, W	150	102.3 **31.8 %**	94.7 **37 %**	126 **16%**
- calorimeter middle section, W	280	180.8 **35.3%**	166.5 **40.5%**	228 **18%**
- calorimeter extreme section, W	-	165.5	126.1	206
Heat fluxes debalance	-	0.024 %	0.6 %	0.3 %

Table 7. Comparison of experimental and computed values. Regime # 2

Parameter	Test	Calculated α=150	Calculated α=0	Calculated, k-ω turbulence model α=150
Power of radiation from the melt surface, W	7000	8915.7 **27.3 %**	8948.4 **27.8 %**	8906 **27%**
Temperature of the melt surface central spot	2180, C	2303, C **5.6 %** **(DT=123 K)**	2308, C **5.8 %** **(DT=128 K)**	2314, C **6 %** **(DT=134 K)**
Crust thickness on the bottom calorimeter, mm	4.5	5.4 **20 %**	2.5 **44 %**	4.6 **2%**
Power from the melt to:				
- crucible, W	21460	20672 **3.7 %**	20622 **3.9 %**	20610 **4%**
- calorimeter central section, W	160	134.7 **15.8 %**	120.7 **20%**	145 **9%**
- calorimeter middle section, W	320	245 **23.4 %**	229.3 **28 %**	276 **14 %**
- calorimeter extreme section, W	-	225	191.8	257
Heat fluxes debalance	-	0.02%	0.28%	0.02%

Table 8. Comparison of experimental and computed values. Regime # 3

Parameter	Test	Calculated α=150	Calculated α=0	Calculated, k-ω turbulence model α=150
Power of radiation from the melt surface, W	7400	5987.7 **19%**	5995.8 **18.9 %**	6733 **9%**
Temperature of the melt surface central spot	2220, C	2101, C **5.3%** **(DT=119 K)**	2076, C **6.4%** **(DT=144 K)**	2163, C **2.5%** **(DT=57 K)**
Crust thickness on the bottom calorimeter, mm	14	10.5 **25 %**	4.4 **68 %**	14.7 **5%**
Power from the melt to:				
- crucible, W	24080	26285 **6.1 %**	26230.3 **8.9 %**	25391 **5.4%**
- calorimeter central section, W	100	87.6 **12.4%**	102.2 **2.2 %**	88 **12%**
- calorimeter middle section, W	230	153.6 **33 %**	182.8 **20.5 %**	153 **33%**
- calorimeter extreme section, W	-	142.3	136.7	142
Heat fluxes debalance	-	0.01%	0.04%	0.46%

Table 9. Comparison of experimental and computed values. Regime # 4

Parameter	Test	Calculated α=150	Calculated α=0	Calculated, k-ω turbulence model α=150
Power of radiation from the melt surface, W	5970	5141.5 **13 %**	5078.5 **14.9 %**	5840 **2%**
Temperature of the melt surface central spot	2090, C	2000, C **4.5 %** **(DT=90 K)**	1984, C **5 %** **(DT=104 K)**	2096, C **0.3%** **(DT=6 K)**
Crust thickness on the bottom calorimeter, mm	14	14.2 **1.4 %**	7.5 **46 %**	11 **21%**
Power from the melt to:				
- crucible, W	19190	20102.8 **4.7 %**	20126.6 **4 %**	19383 **1%**
- calorimeter central section, W	95	63.2 **33 %**	71.6 **24%**	63 **34%**
- calorimeter middle section, W	-	110.5	120.8	110
- calorimeter extreme section, W	-	104	91.24	104
Heat fluxes debalance	-	0.01%	0.1 %	0.08%

Deviation of the results of 2D calculations from experimental data is shown in Tab. 10.

Table 10. Deviation of results of 2D calculations from experimental data

Parameter	Deviation, % α=150	Deviation,% α=0	Deviation, % k-ω turbulence model α=150
Power of radiation from the melt surface, W	14 (#1) 27.3 (#2) 19 (#3) 13 (#4)	14 (#1) 27.8 (#2) 18.9 (#3) 14.9 (#4)	4.2 (#1) 27 (#2) 9 (#3) 2 (#4)
Temperature of the melt surface central spot	4.7 (#1) **(DT= - 97 K)** 5.6 (#2) **(DT= 123 K)** 5.3 (#3) **(DT= - 119 K)** 4.5 (#4) **(DT= - 90 K)**	5.1 (#1) **(DT= - 104 K)** 5.8 (#2) **(DT= 128 K)** 6.4 (#3) **(DT= - 144 K)** 5 (#4) **(DT= - 104 K)**	0.9 (#1) **(DT= - 18 K)** 6 (#2) **(DT= 134 K)** 2.5 (#3) **(DT= - 57 K)** 0.3 (#4) **(DT= 6 K)**
Crust thickness on the bottom calorimeter, mm	50 (#1) 20 (#2) 25 (#3) 1.4 (#4)	29 (#1) 44 (#2) 68 (#3) 46 (#4)	21 (#1) 2 (#2) 5 (#3) 21 (#4)
Power from the melt to:			
- crucible, W	10 (#1) 3.7 (#2) 6.1 (#3) 4.7 (#4)	11 (#1) 3.9 (#2) 8.9 (#3) 4 (#4)	5.5 (#1) 4 (#2) 5.4 (#3) 1 (#4)
- calorimeter central section, W	31.8 (#1) 15.8 (#2) 12.4 (#3) 33 (#4)	37 (#1) 20 (#2) 2.2 (#3) 24 (#4)	16 (#1) 9 (#2) 12 (#3) 34 (#4)
- calorimeter middle section, W	35.5 (#1) 23.4 (#2) 33 (#3)	40.5 (#1) 28 (#2) 20.5 (#3)	18 (#1) 14 (#2) 33 (#3)
Heat fluxes debalance	0.01 ÷ 0.024	0.04 ÷ 0.6	0.02 ÷ 0.46

It can be seen from Tab. 10 that in the course of direct modeling of turbulence the transition from α = 150 W/(m^2·K) to α = 0 has reduced thickness of the crust on the bottom calorimeter and this has noticeably decreased accuracy of its calculation for three regimes (##2÷4) of MC4. The accuracy of heat fluxes and temperature calculations has changed less significantly. The decrease of the calculated crust thickness on the lower calorimeter at α = 0 was caused by the temperature rise in the bottom part of the melt. It should be noted that there is ambiguity in the effect of α = 150 W/(m^2·K) → α = 0 transition on the precision of heat fluxes calculation, i.e., it can either increase, or decrease. It relates to the features of changes in the flow structure, which consists of a system of evolving vortexes (Fig. 17).

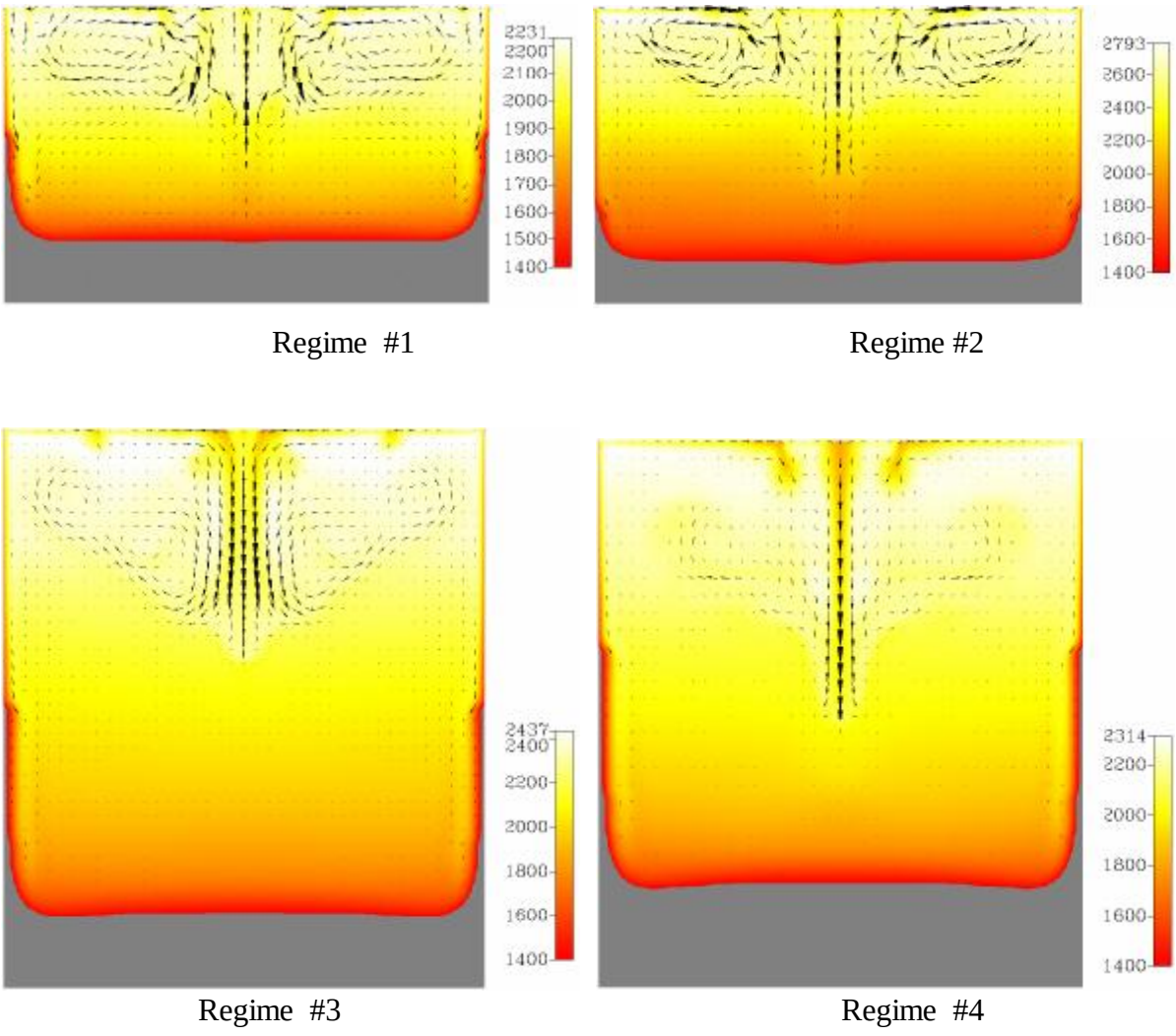

Fig. 17. Temperature (^{o}C) and velocity vector distribution during regimes #1¸4 in MC4. Solved using the nonstationary system of Navier-Stokes equations

Fig. 18 shows the momentary distribution of the velocity absolute value during regime #1 in MC4. The velocity peak (V_{max}) equals 3.47 cm/s; it is localized in the upper part of the melt near the axis in the downward stream. The distribution of velocity across the free surface is nonuniform; in some areas zero velocity is observed, and it is there that radiation cools the melt noticeably.

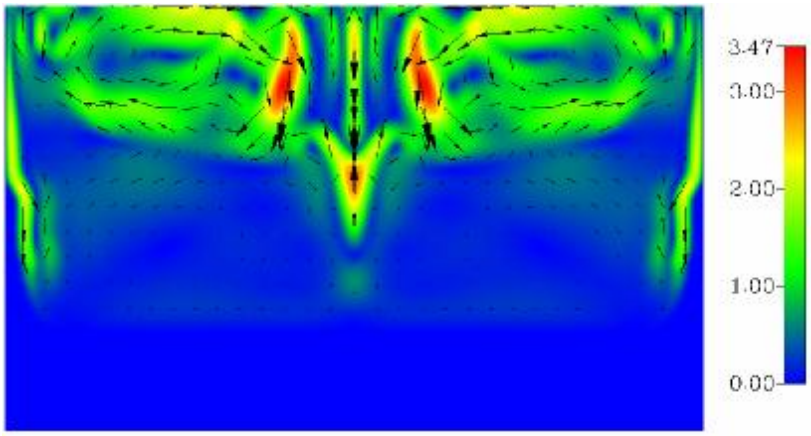

Fig. 18. Velocity absolute value (cm/s) and velocity vectors distribution during regime #1 in MC4

It was shown above that the application of the k-ω turbulence model to the majority of the considered regimes of MC4 made calculations of heat fluxes, temperature and crust thickness more precise. However, this model reduces the nonstationary flow to the stationary one with a simplified flow structure. Indeed, a complex vortex flow with intensive convection in the molten pool upper part (Fig. 17), which can be solved using the nonstationary system of Navier-Stokes equations, becomes transformed into a single toroidal vortex flow (Fig. 19) when the k-ω turbulence model is applied. This effect is due to the nature of the turbulence model which uses the averaged characteristics.

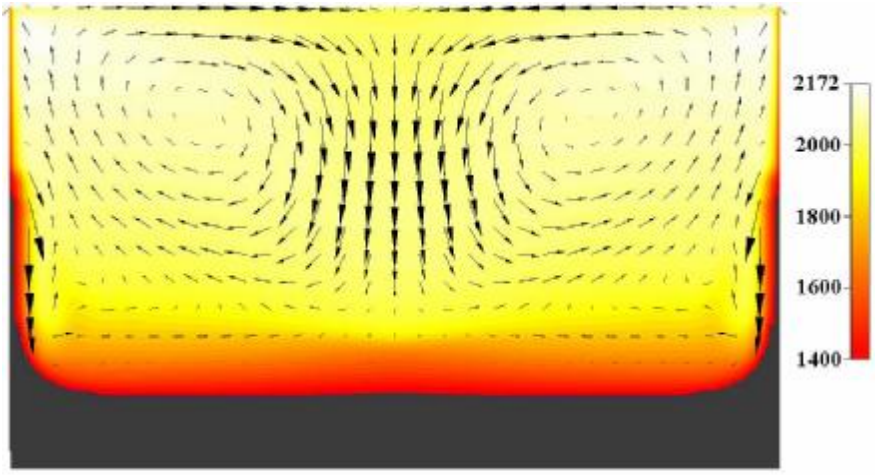

Fig. 19. Temperature (^{o}C) and velocity vector distribution during regime #1 in MC4. Solved using the k-w turbulence model

Fig. 20 shows the momentary radial distribution of temperature in the melt during regime #4 in MC4 when the direct turbulence modeling is applied. It may be seen that the maximum radial nonuniformity of temperature is on the melt free surface (h=79 mm), while this surface temperature is lower than that of the underlayer (h=70 mm), it being determined by the surface cooling through radiation. Deeper into the melt, the radial nonuniformity of temperature reduces, excluding the lateral layer that gives heat to the crucible.

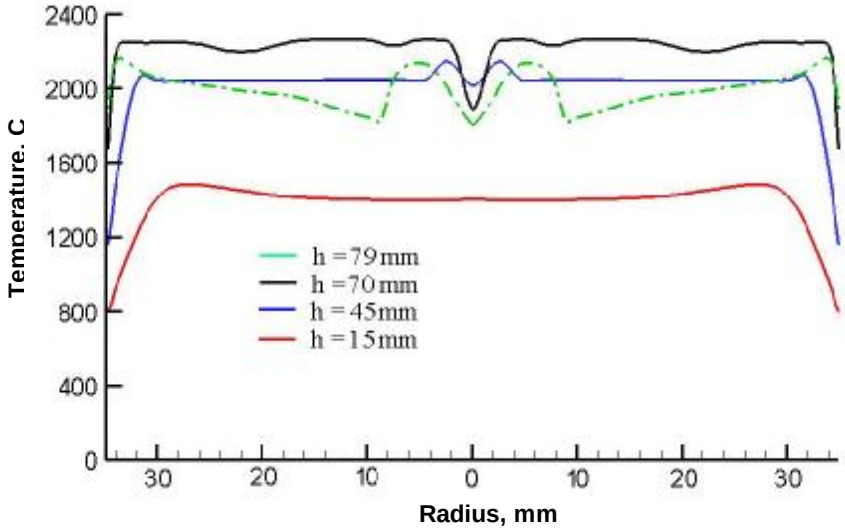

Fig. 20. Temperature radial distribution at different distances from the molten pool bottom, Regime # 4 in MC4

Fig. 21 shows the momentary heightwise temperature distribution in the melt during regime #4 in MC4 when the direct turbulence modeling is applied. Near the crucible (r = 35 mm) the melt temperature is below T_L along the total height.

On the axis (r = 0) there may be seen a section (at half the melt height) where the temperature increases monotonically as the distance from the free surface grows. This effect is caused by the nature of free convective flow: the cooled part of the melt descends (from the free surface center in this case) and warms up on its way from the laterally positioned heat sources. After the peak temperature has been reached locally, the further cooling of the melt as the height decreases would be caused by heat removal by the bottom calorimeter.

Starting from the radius of 20 mm and up to the crucible, the temperature monotonically reduces as the height decreases (excluding the subsurface layer which is influenced by the surface cooling through radiation).

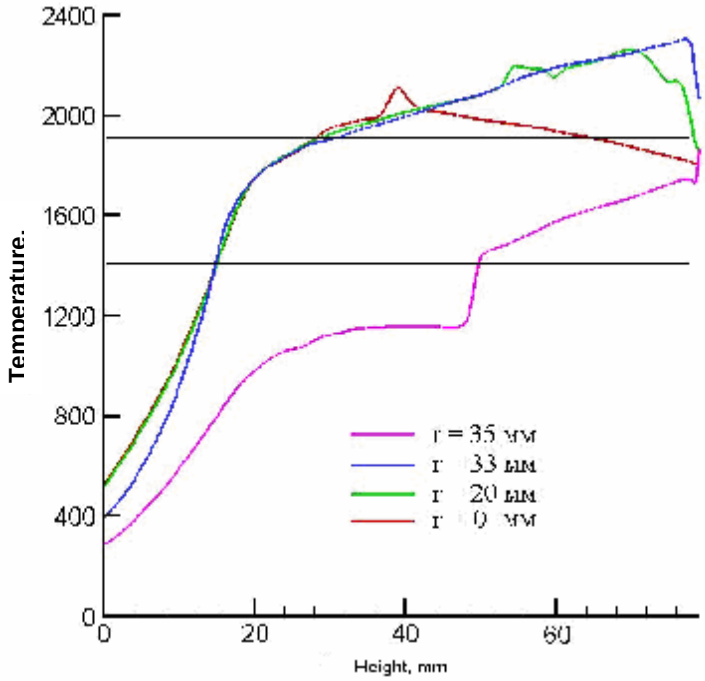

Fig. 21. Heightwise temperature distribution at different distances from the axis. Regime #4 in MC4

Fig. 22 shows the momentary distribution of heat flux density along the radius of the three-section bottom calorimeter. The peak heat flux density is realized in the calorimeter center; it is the highest for regime #2 and is close to 0.2 MW, and it's the lowest, around 0.09 MW, under regime #4.

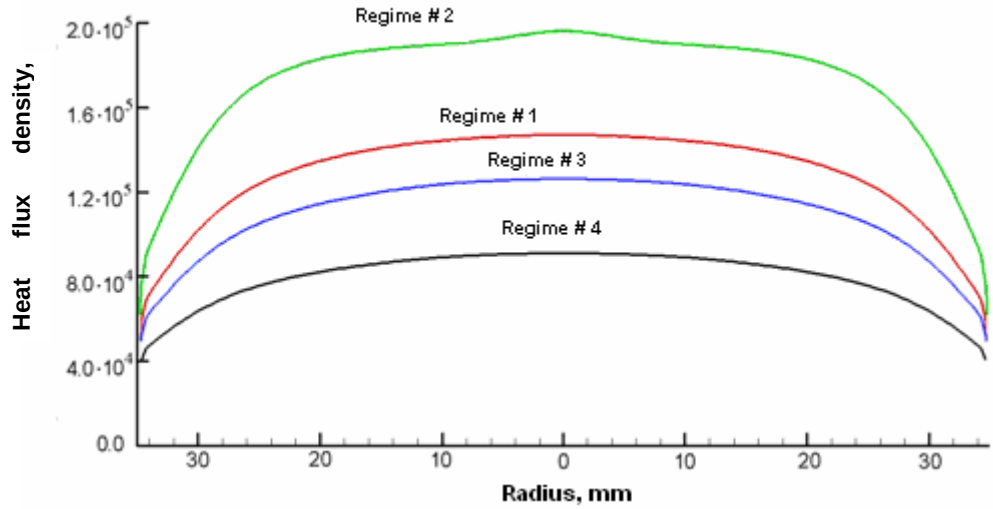

Fig. 22. Heat flux density distribution along the bottom calorimeter radius. Regimes #1¸4 in MC4

Fig. 23 shows heat flux densities normalized by the values in the calorimeter center. Obviously, regardless of the significant difference between the absolute values, profiles of the normalized flows have similarity.

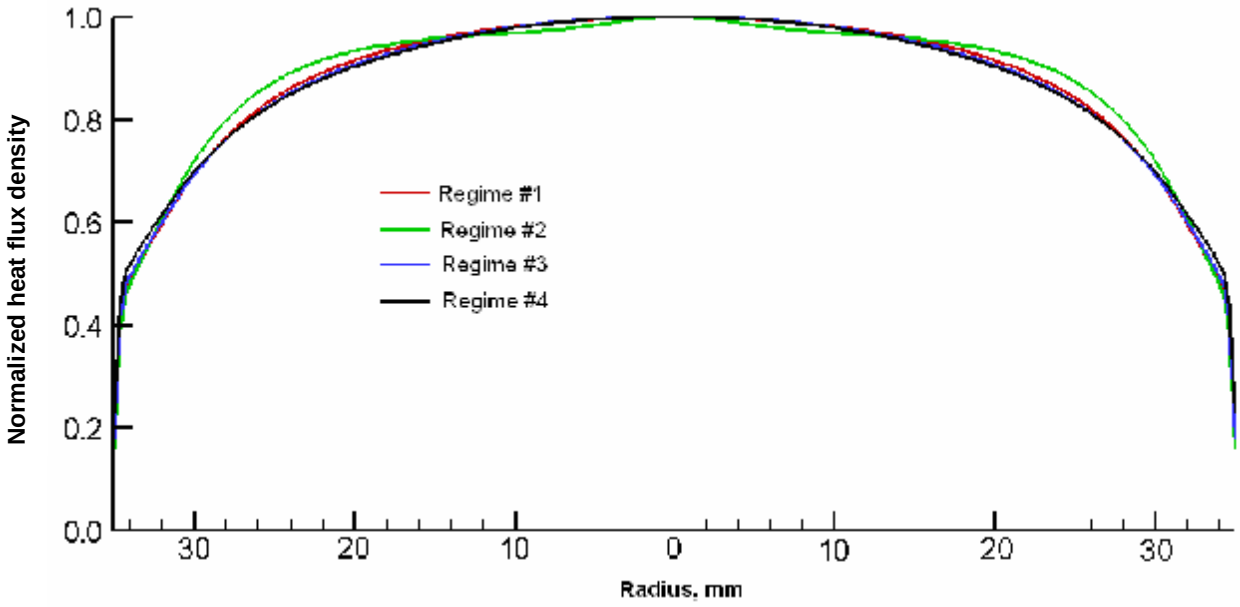

Fig. 23. Distribution along the bottom calorimeter radius of the heat flux density normalized by the value in the calorimeter center (regimes #1¸4 in MC4)

The figures below relate to the use of the k-ω turbulence model used for assessing the Kolmogorov scale of turbulence.

From Fig. 24 that shows the turbulent energy dissipation rate distribution it is seen that the peak ε value is localized at the axis in the melt upper part. The calculation using (15) shows that in this zone the value of the Kolmogorov scale of turbulence is minimal (η_{min}=0.19 mm), while in other parts of the melt η varies within the 0.19<η<0.7 mm range at T>T_{liq} (Fig. 25). A sharp increase of η happens at the melt solidification near the low-temperature walls (T<T_{liq}).

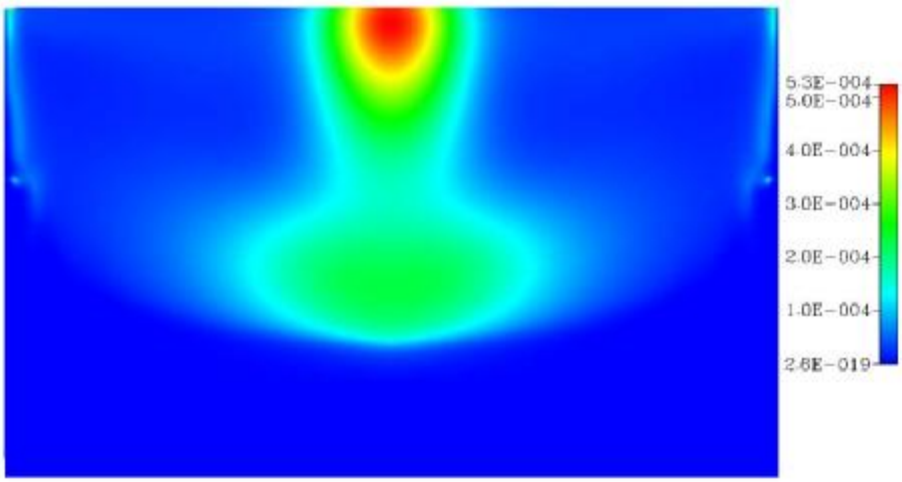

Fig. 24. Kinetic turbulent energy dissipation rate, m^2/s^3 (MC4 #1)

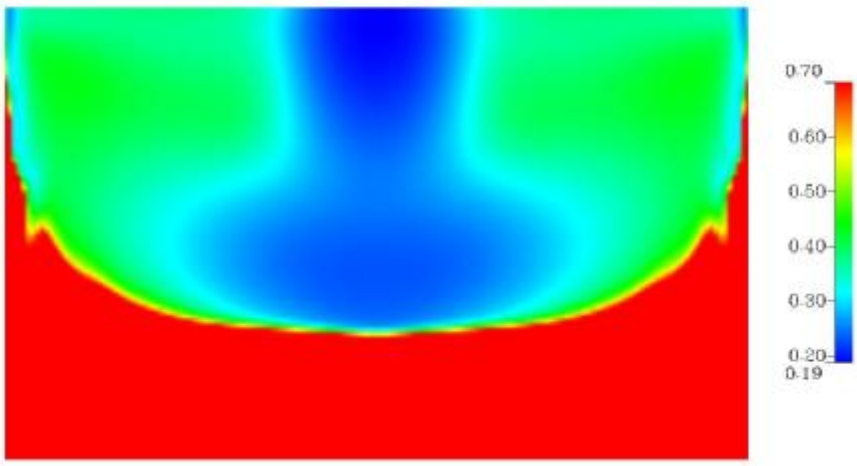

Fig. 25. Kolmogorov scale of turbulence, mm (MC4 #1)

The size of cells in the used computational grid is about 0.4 mm, therefore in the considerable part of the melt the Kolmogorov scale is above this value and only twice smaller near the computational domain axis. This confirms applicability of direct numerical modeling of turbulence in MC4. It should be reminded that it provided acceptable agreement between the calculated and experimental data on heat fluxes, free surface temperature and crust thickness on the bottom calorimeter. Also important is that it finds a solution to the vortex structure of the flow.

Application of the k-ω turbulence model, in its turn, has added precision to the calculation of most parameters, but significantly simplified structure of the free convective flow.

Peculiarity of the given melt calculations in proximity to the crucible tubes is notable. That is, at some height along the computational domain lateral boundary, which models the crucible surface, the calculated temperature is above T_{Sol} though below T_{Liq} ($T_{Sol}<T<T_{Liq}$) (Fig. 20). A $T<T_{Sol}$ would be natural to expect at the lateral boundary, as a liquid phase cannot maintain the melt boundary vertical.

This disagreement may be explained by the incompleteness of modeling the 3D melt boundary near the crucible. Indeed, the real boundary formed by the crucible tubes is not uniform and, theoretically, there may be gaps in the solid phase on it though shape would be conserved, as a liquid may keep fixed over the gaps due to a very strong surface tension (about 0.6 H/m [10]). This does not contradict to the results of the lateral crust inspection after MC4, which showed the presence of areas with minor crust thickness bordering on a relatively thick crust that had formed in the gaps between the tubes. The lateral boundary of the accepted computational geometry is cylindrical, and on it we obtain an averaged temperature, which at some height falls within the $T_{Sol}<T<T_{Liq}$ range. Despite the mentioned gaps in the solid phase on the real lateral boundary, a model may use the condition of adhesion due to the small effective area of the gaps.

The setting of boundary conditions for the melt/crucible lateral boundary may be simplified by using the $T=T_{Sol}$ condition of the first kind. The influence of this condition, as well as of the condition $T=T_{Liq}$ on the results of calculations are analyzed in Appendix 1.

3.2. Three-dimensional calculations

Fig. 26 shows a 3D computational grid containing about 600 000 cells.

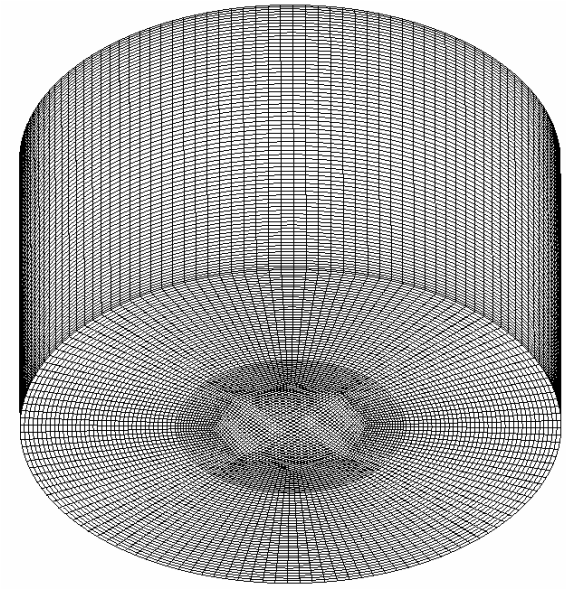

Fig. 26. Computational grid

Calculations were made for regime #1 of MC4 using the nonstationary system of Navier-Stokes equations (1)÷(5) with the temperature boundary condition (23) at $\alpha = 0$.

The results of computations are given in Tab. 11; the disagreement with the heat flux experimental data is satisfactory and does not exceed 30 %.

Table 11. Computations for regime #1 in MC4

Parameter	Test	Calculated 2D α=0	Calculated 3D α=0
Power of radiation from the melt surface, W	5300	4645 **14%**	4537 **15%**
Temperature of the melt surface central spot	2025, C	1921, C **5.1%**	1918, C **5.2% (107 C)**
Crust thickness on the bottom calorimeter, mm	5.5	3.9 **29%**	5.35 **2.7%**
Power from the melt to:			
- crucible, W	10200	11211.7 **11 %**	11098 **8.8%**
- calorimeter central section, W	150	94.7 **37 %**	97.9 **35%**
- calorimeter middle section, W	280	166.5 **40.5%**	174.4 **37%**

Fig. 27 shows the melt free surface and temperature fields that reflect vortex structure of the stream. Obviously, the size and shape of the calculated large-scale formations is analogous to the experimental ones.

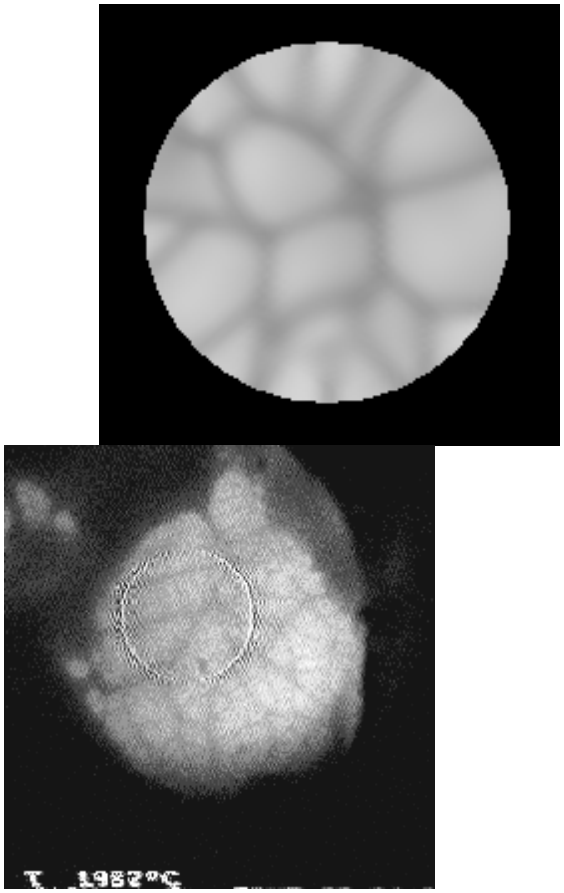

Calculated **Test**

Fig. 27. Temperature distribution in the melt free surface central spot Ø 21 mm.

Fig. 28 shows the momentary distribution of the melt velocity on the free surface. The calculated maximum velocity equals 2.66 cm/s, it being 50% less than the peak experimental value which is 4 cm/s (Tab. 12).

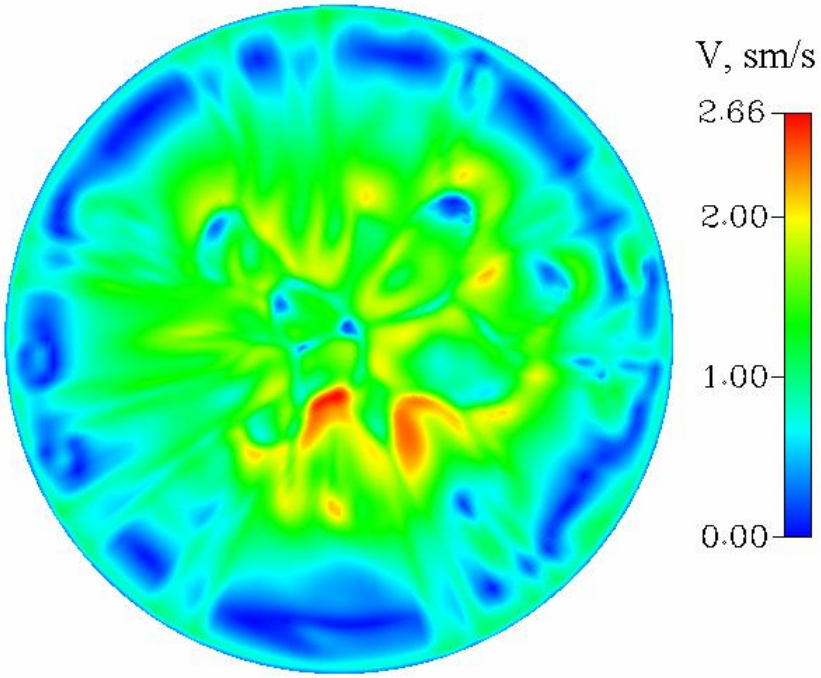

Fig. 28. Velocity distribution on the melt free surface

Table 12

Particle velocity, cm/s, and its direction	**3.5 NW**	**3.2 SE**	**3.2 W**	**1.6 W**	**1.6 S**	**4.0 S**	**4.0 E**	**2.4 SW**	**3.2 W**	**4.0 S**	**0.8 SE**
Distance from the top, mm	8	13	7.8	7.8	11,5	15	21	6	6	16	12
Distance from the left edge, mm	5	1.4	3	2.1	0.3	3.1	1.1	9	11	25	29

Fig. 29 shows temperature distribution on the free surface and along the melt vertical plane recorded at Δt=0.25 s. The peak temperature in bulk melt is observed near the crucible in the pool upper part, it being determined by the heat sources distribution (Fig. 7).

Calculations have indicated two areas in the melt where the descending flow dominates. The first of them is the peripheral area, several millimeters thick, located in proximity to the crucible. The descending flow in it is caused by cooling of the melt by the crucible. The second one – the central area – is depicted in the figures as a leaf with a dynamically changing shape. The downward movement in it is determined by the minimum power supply near the axis, and a temperature lower than at the boundaries due to the surface cooling through radiation. Volume electromagnetic forces in MC4 are insignificant, therefore the flow structure is determined by the buoyancy forces. A considerable downward movement along the axis

entrains the melt from the free surface to the center.

The downward axial flow attenuates soon after it passes the liquidus boundary due to the sharply increasing viscosity.

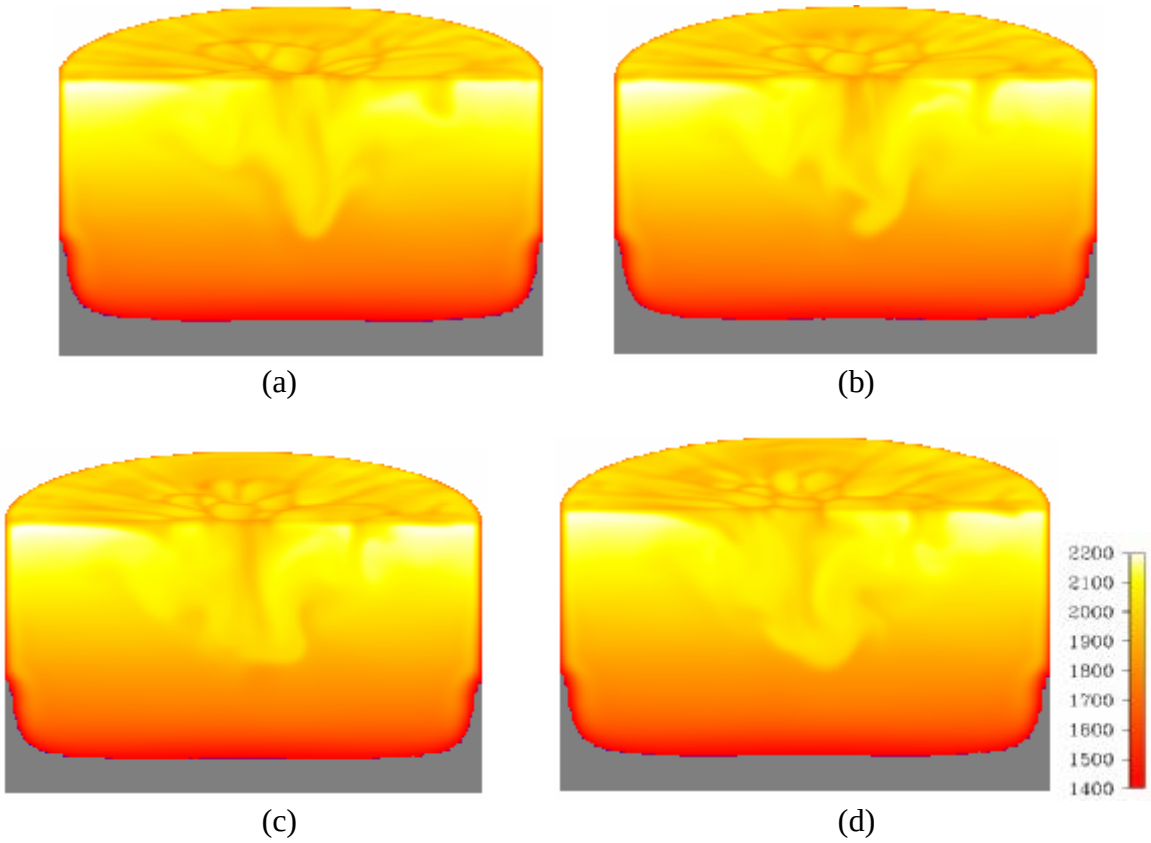

Fig. 29. Dynamics of temperature (°C) change across the vertical plane and on a half of the melt free surface

Time step is 0.25 s. Sequence: left-right, top-down. The melt crust is grey.

Fig. 30 shows the momentary temperature radial distribution in the melt. Obviously, the maximum radial temperature nonuniformity is observed on the free surface due to the intensive heat radiation into the environment, when the delay of a liquid element near the surface leads to rapid cooling, and the emergence of a liquid element from below yields a local rise of temperature.

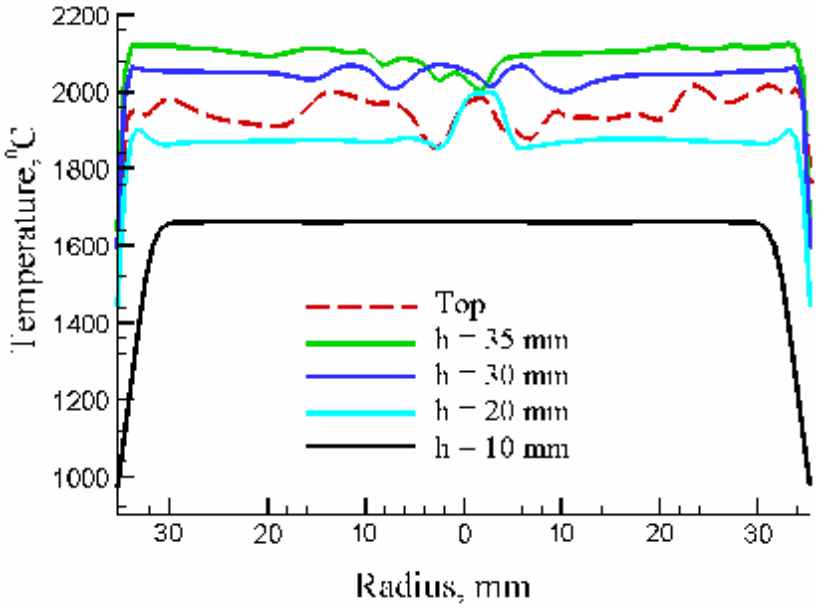

Fig. 30. Momentary radial temperature distribution at different height (h) from the pool bottom

Fig. 31 shows the momentary heightwise temperature distribution along radiuses in the melt. Regardless of the radius, a shift from the free surface 2-3 mm deeper into the melt would first show a sharp temperature rise for about 250 K and then temperature lowering at the decrease of height. Along the melt axis (r=0), the temperature is undergoing a nonmonotonic change up to the T_{Liq} level.

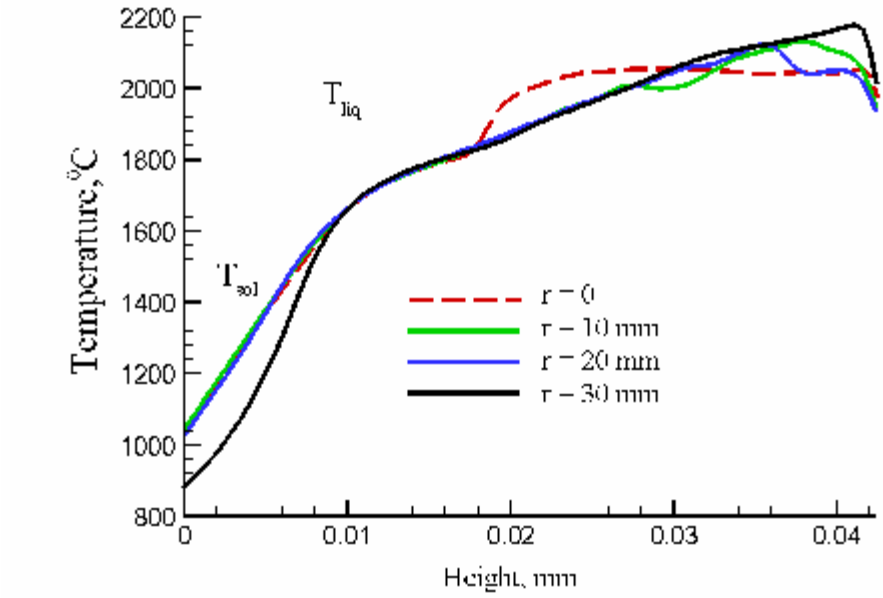

Fig. 31. Momentary heightwise temperature distribution in the pool along different radiuses (r)

Finally, proceeding from the agreement between the calculated and experimental data on heat fluxes and the free surface structure, verification of the model and DYMELT code using the

MC4 data can be regarded as satisfactory.

4. Results of computations for MC5

The difference of MC5 tests from MC4 is in the replacement of the bottom calorimeter with the steel specimen, as in MC5 the specimen surface corrosion at the contact with C-100 corium was investigated.

In Section 1.3 it was noted that the electromagnetic forces in MC5 were about an order of magnitude stronger than in MC4. Besides, the skin layer was thicker in MC5 at 0.13 MHz inductor frequency, i.e. an order of magnitude smaller than in MC4. This has lead to significant changes in the free convective flow structure in MC5 compared to MC4.

This Section offers the results of molten corium numerical modeling in MC5 using the nonstationary system of Navier-Stokes equations. In a 2D approximation, the problem has been solved taking into account the conjugated heat exchange between the specimen and corium. Hydrodynamics was the only subject of 3D calculations, because the experimental temperature distribution along the specimen radius was specified for the lower boundary between corium and specimen.

4.1. Two-dimensional calculations

The computational domain is shown in Fig. 32. Among its components are the melt, specimen, layers of fianite and ZrO_2 powder, and a simulator of the gaseous above-melt atmosphere (in the present approximation – a stationary transparent medium with thermal conductivity and heat capacity of air).

The model assumed the following boundary conditions:

- T_w = 320 K at the outer boundaries of the gaseous medium simulator;
- T_w = 310 K at the conjugation boundaries between the specimen and calorimeters;
- Heat exchange through radiation and thermal conductivity (23) at T_w=320 K and α = 50 W/(m^2·K) at the boundaries of the crucible with corium, and with the ZrO_2 powder and fianite;
- Conjugated heat exchange (26) at the corium/specimen boundary;
- Adhesion condition of u = v = 0 at the boundaries of corium with the crucible and specimen;
- The gliding condition of v = 0, $\partial u/\partial n$ =0 at the corium upper boundary.

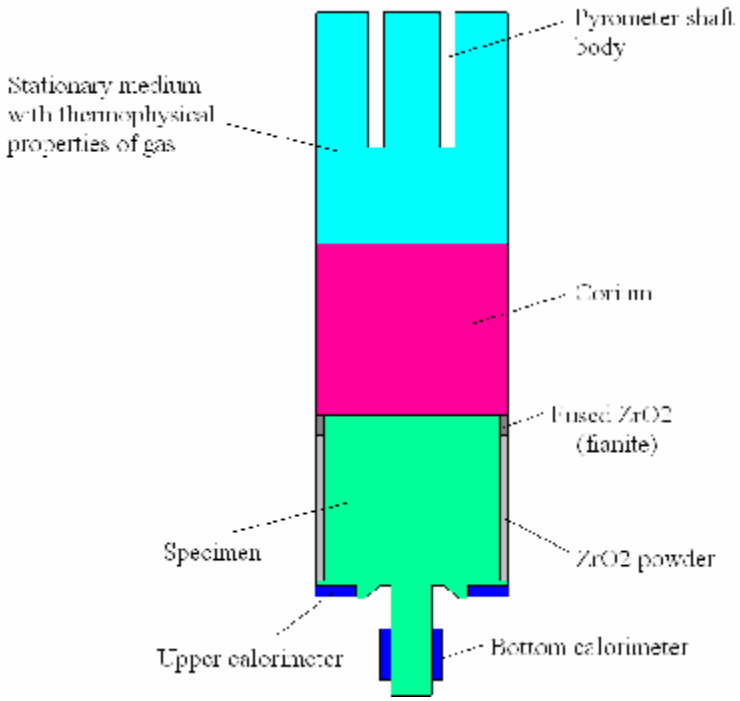

Fig. 32. Computational domain diagram in MC5

Fig. 33 shows the distribution of temperature in corium, lateral skull, specimen and a part of the gaseous medium simulator during regime #1 in MC5. It may be seen that the radial distribution of temperature is more uniform in the specimen than in corium due to high thermal conductivity of steel. At the same time, the radial nonuniformity of the free surface temperature has caused a considerable radial nonuniformity of temperature in the layer of the gaseous medium simulator adjacent to the melt. Therefore, the coordinated calculation of the free convective gas movement should take into consideration the temperature field structure at the melt surface.

T_{ev}, the calculated melt free surface temperature, averaged for a Ø 4 mm circle using formula (30), was 2563 K, i.e. 40 K less than in the test.

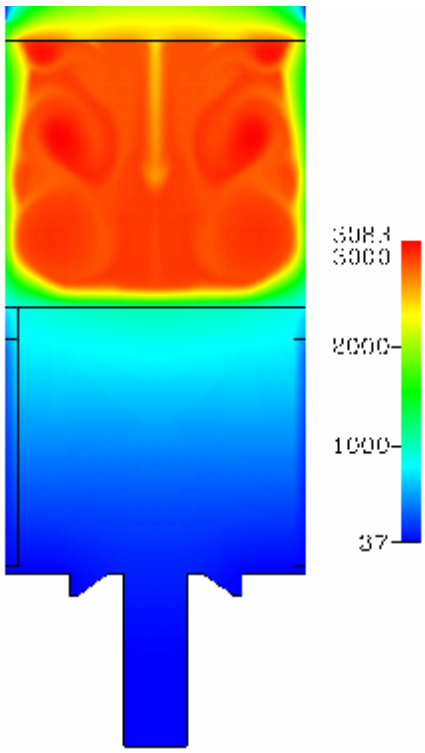

Fig. 33. Temperature (^{o}C) distribution, regime #1

Fig. 34 shows velocity and temperature fields in the molten pool for the instants of time differing from each other by $\Delta t = 1$ s under the established quasiequilibrium condition of the system. The corium crust is given in grey colour. It may be seen that peak temperatures are located at the melt upper part periphery, and for the said instants of time T_{max} was 3061; 3008 and 3072°C, respectively. This pretty rapid change of the peak temperature is caused by the flow nonstationary structure, which is represented in the given 2D formulation by three toroidal vortexes.

A small upper vortex surrounds the zone of the absolute peak temperature of the melt. It is created by the electromagnetic force, which is directed towards the axis and pool bottom, and is at its peak in this part of the melt (Appendix 2 demonstrates the significant influence of the electromagnetic forces on the melt condition in MC5).

The lower vortex has the maximum size. The flow spinning in it is caused by the radial spreading of the downstream near the bottom crust and the following turn of the flow upwards in the pool corner. This vortex shows the maximum velocity, which can be explained by acceleration in a stream of incompressible liquid at lessening of its cross-section during the turn at the molten pool lower corner, as in the present case.

The medium vortex changes its position and shape more dynamically than the upper and lower vortexes, as it is located between them.

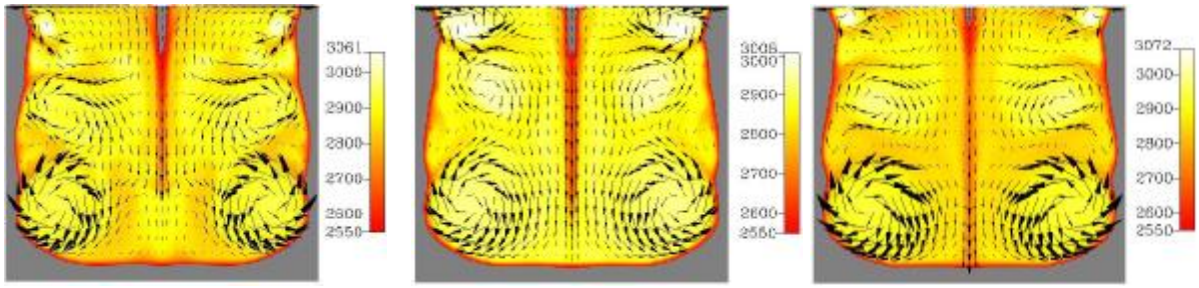

(a) (b) (c)

Fig. 34. Velocity vectors and corium temperature (°C), Dt = 1 s, regime #1

Fig. 35 shows the velocity absolute value distribution at Δt = 1 s. In Fig. 35(b) the corium near the free surface moves upwards excluding the solid fraction along the axis, and in Fig. 35(c) it moves downwards. Such a frequent change in the flow direction correlates with observations of the melt surface which changes in MC5 more dynamically and unpredictably than in MC4. The differences may be caused by the above-mentioned noticeable effect of electromagnetic forces in MC5. A comparison of velocities in MC4 and MC5 (Figs. 18 and 35) shows the melt peak velocity in MC5 to be several times higher.

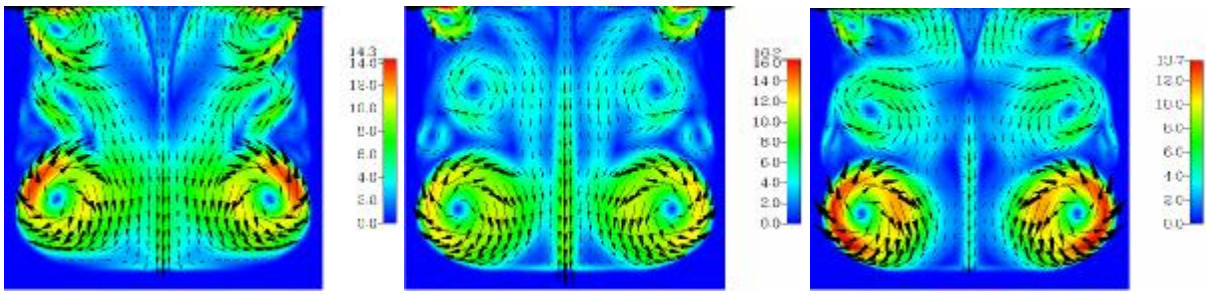

(a) (b) (c)

Fig. 35. Velocity absolute value (cm/s) and vectors, Dt = 1 s, regime #1

Fig. 36 shows the crust shapes for the considered three time instants. The differences along the melt edges are hardly noticeable. A small isle of solid fraction in the free surface center has formed as a result of melt cooling through radiation at the deceleration of liquid near the central point (characteristic for the 2D geometry).

The calculated thickness (h_{comp}) of the corium lower crust above the specimen center during regime #1 in MC5 was 3.2 mm, while the experimental value (h_{exp}) was 3 mm.

(a) (b) (c)

Fig. 36. Corium crust, Dt = 1 s, regime #1

The distribution of density of the heat flux to the specimen during regime #1 in MC5 is shown in Fig. 37 for the time instants corresponding to (a, b) in Fig. 35. The maximum heat flux density (q) is seen to be in the center and approximately equal 1 MW/m^2. Away from the axis, the value of heat flux density diminishes, and this decrease becomes noticeably faster at R>20 mm because of the lower crust thickening. Starting from R=14 mm, heat fluxes for the time instants (a) and (b) are identical. Their difference in the specimen surface central part before R=14 mm relates to fluctuation of the axial flow parameters, however, as Fig. 35 shows, a lower heat flux value corresponds to a higher velocity of the downflow. Direct correlation is absent due to the inertia of the process in the specimen/corium/crust system. The heat flux drops sharply at R=32 mm because of the transition from the specimen to fianite.

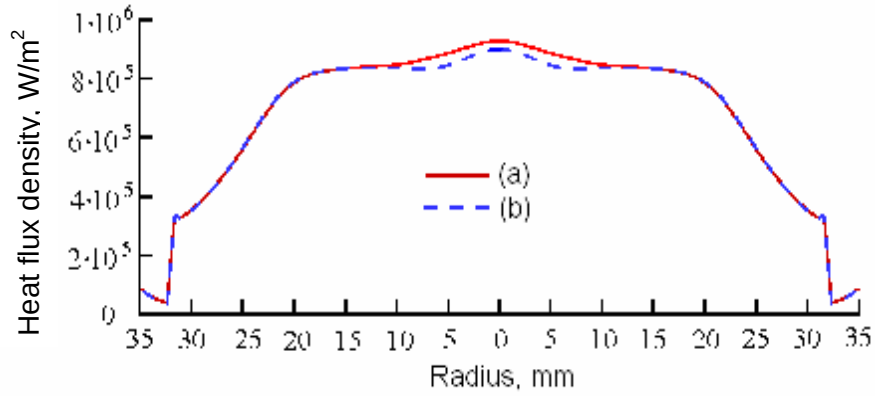

Fig. 37. Radial distribution of density of the heat flux from corium to the specimen, regime #1

The flux to the specimen forms the temperature distribution, a 2D image of which is given in Fig. 38. The radial distribution of temperatures are shown in Fig. 39. The specimen center is seen to be superheated relative to the edges. This superheating decreases away from the specimen top. For instance, at Δh=0.5 mm the temperature difference between the center and edges equals 167 K, and at Δh=2 mm ΔT=144 K. The high radial temperature gradient in fianite is due to low thermal conductivity.

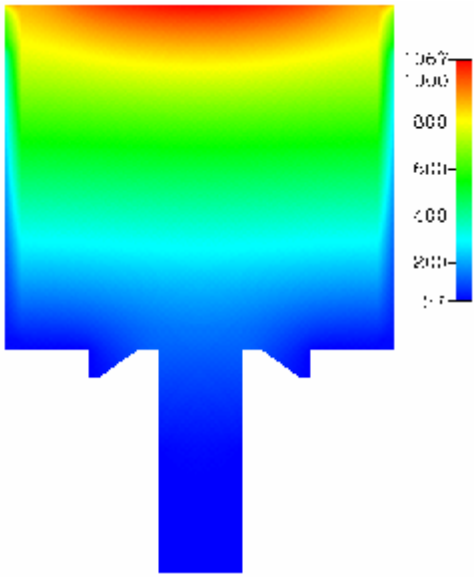

Fig. 38. Temperature (° C) distribution in the specimen, regime #1

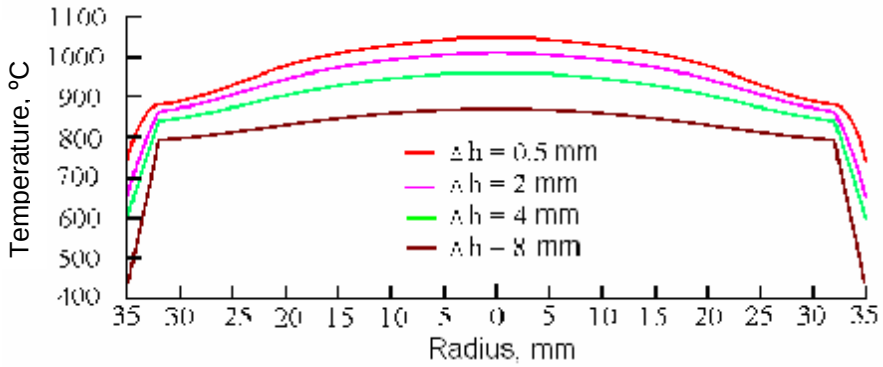

Fig. 39. Temperature distribution along the radius of the specimen and lateral skull at different distances (Dh) from the specimen upper top, regime #1

Tab. 13 summarizes regimes ##1÷4 parameters, as well as the calculated and experimental values of crust thickness above the specimen (their satisfactory agreement is obvious).

Table 13. Regimes ##1¸4parameters

Regime No.	Time from melting start, s	Pool height, mm	Crust thickness above the specimen center, mm **Test**	Crust thickness above the specimen center, mm **Calculated**	Heat generation in the melt [3], KW
1	22615	59	**3.0**	**3.3**	20.16
2	60303	60	**2.75**	**3.3**	21.98
3	91052	64	**2.75**	**4**	21.55
4	132811	58	**2.75**	**3.15**	21.31

In MC5, the specimen temperature was measured in the points which coordinates are given in Tab. 14.

Table 14. Points of the specimen temperature measurements

Thermocouple	r, mm (distance from junction to the specimen axis)	h, mm (from the melt-facing top)
TC01	10	0
TC02	10	2
TC03	10	4
TC04	10	6
TC05	10	6
TC06	10	8
TC07	10	15
TC08	29	0
TC09	29	2
TC10	29	15
TC11	29	40
TC12	29	101.7
TC13	7.5	

The history of thermocouple readings is given in Fig. 40.

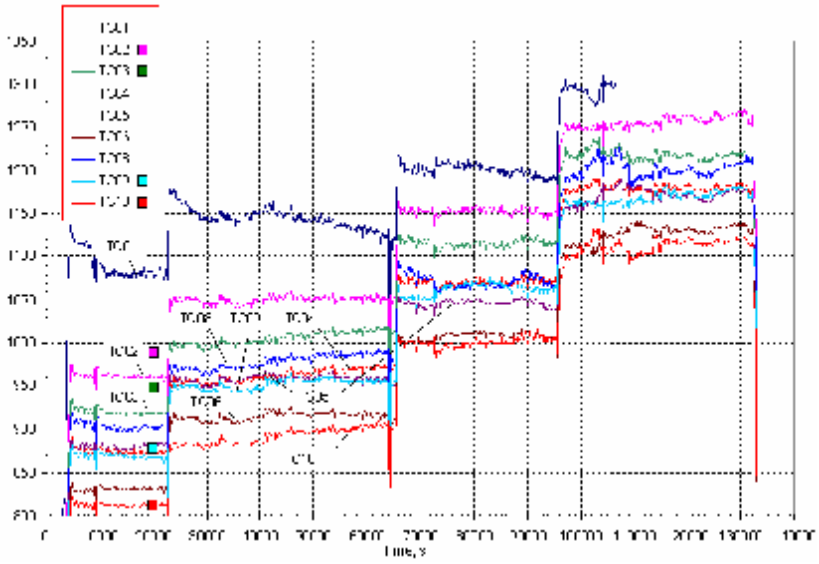

Fig. 40. Thermocouple readings in MC5

Figs. 41÷44 compare the experimental and calculated heightwise temperature distribution in the specimen during regimes ##1÷4. It can be seen that satisfactory agreement is observed only for regimes ##1÷2. For regimes ##3÷4, the calculated values are much lower than the experimental ones. This can be explained by changes in the above-melt conditions which were disregarded in the present calculations: for instance, an above-melt crust that started forming during regime #3 and completely covered the free surface during regime #4.

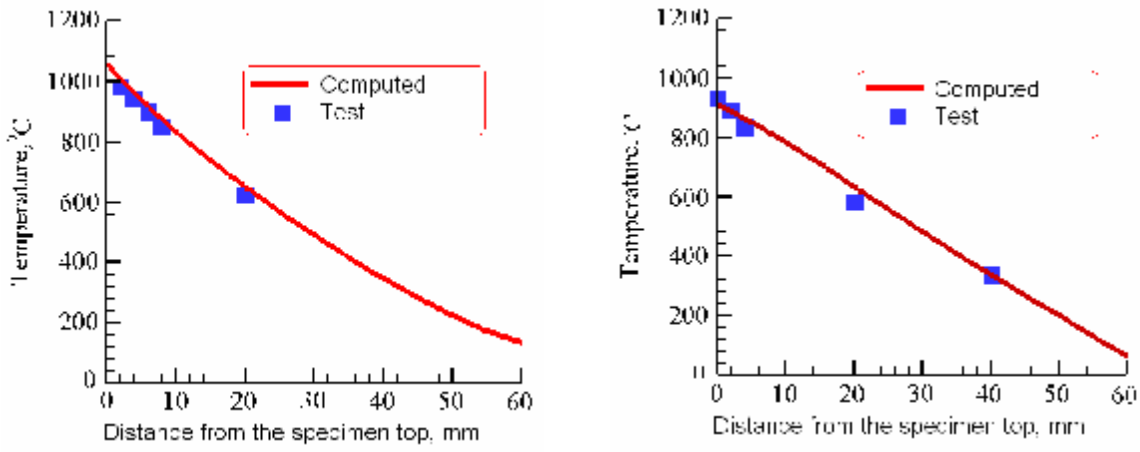

(a) (b)

Fig. 41. Heightwise temperature distribution, 10 mm (a) and 29 mm (b) off the axis, regime #1

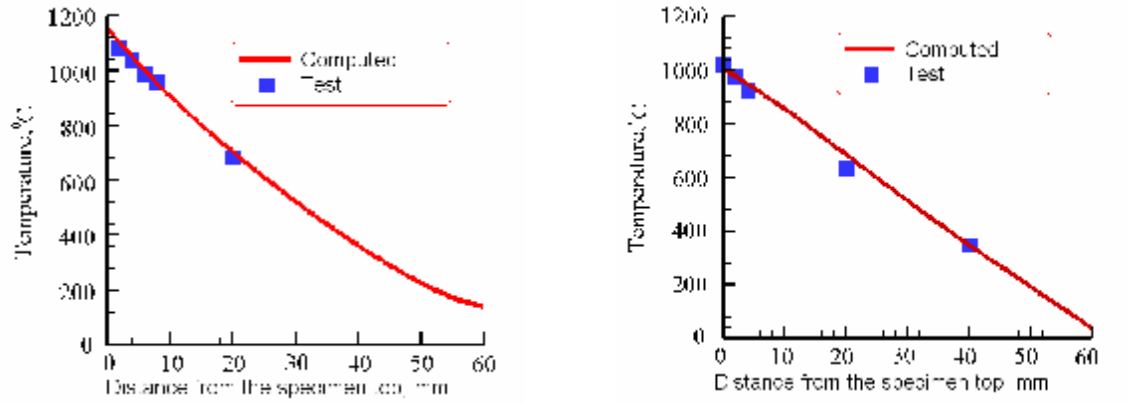

(a) (b)

Fig. 42. Heightwise temperature distribution, 10 mm (a) and 29 mm (b) off the axis, regime #2

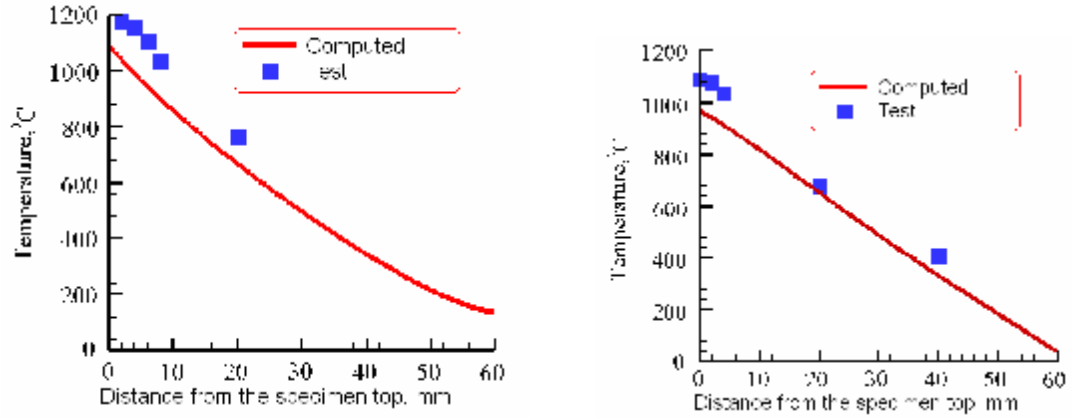

(a) (b)

Fig. 43. Heightwise temperature distribution, 10 mm (a) and 29 mm (b) off the axis, regime #3

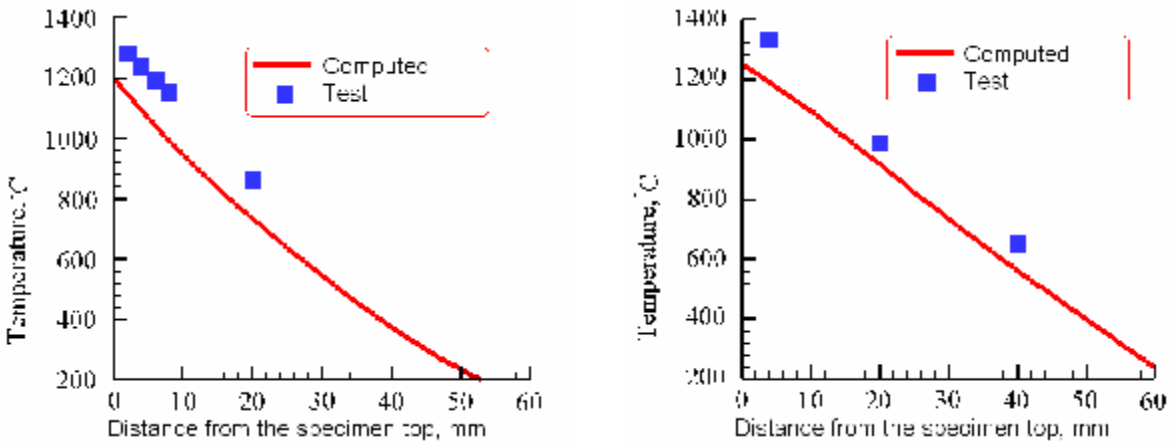

Fig. 44. Heightwise temperature distribution, 10 mm (a) and 29 mm (b) off the axis, regime #4

Fig. 45 shows time dependence of the calculated temperature at 3 points in the specimen which correspond to the location of thermocouples TC02, TC04 and TC09. Zero time corresponds to some nonsteady state; a quasistationary state is attained 250 s later and then temperature fluctuations at δT of about 10°C are observed. These fluctuations are caused by thermal instability of the specimen/corium system in a quasiequilibrium state. The maximum rate of temperature change (δT/δt) is about 0.5 K/s.

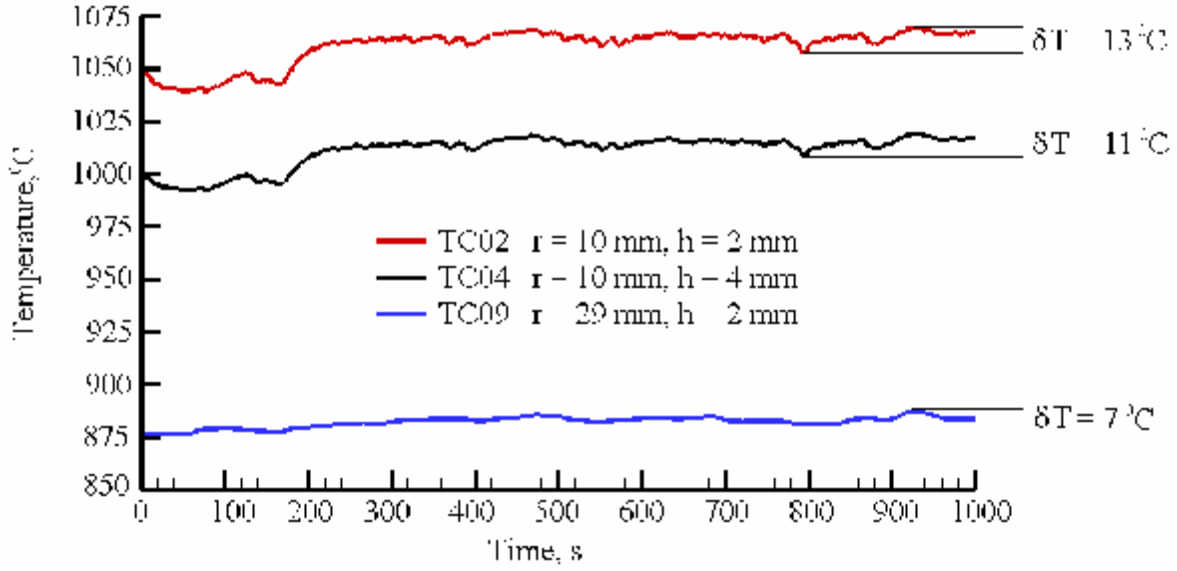

r – distance from the axis; h – distance from the specimen surface

Fig. 45. Calculated time-dependent temperatures at locations of 3 thermocouples in the specimen, regime #1

4.2. Three-dimensional calculations

The 3D calculations for regime #1 of MC5 have been performed using the complete system of Navier-Stokes equations (1)÷(5) and a computational grid analog of that given in Fig. 12. The temperature distribution in the stationary gas above the melt has been calculated. The radial temperature distribution obtained by means of 2D calculations has been specified for the pool bottom. Boundary conditions for other surfaces were the same as in 2D calculations.

Fig. 46 shows a 3D crust boundary with the liquid phase and – for comparison – a crust resulting from 2D calculations. Obviously, shapes of the crusts are similar. Crust thickness above the specimen center was 6.4 mm according to 3D calculations, 3.3 mm by 2D calculations and 3 mm in the test.

Fig. 46. Crust surface bordering on the melt

Fig. 47 illustrates temperature distribution across the melt free surface taken at Δt=0.5 s. From a comparison with Fig. 29 it may be concluded that the melt surface appearance is changing more dynamically in MC5 than in MC4. Besides, the boundaries of large-scale structures are less distinct in MC5 than in MC4, and this agrees well with a video of the melt surface.

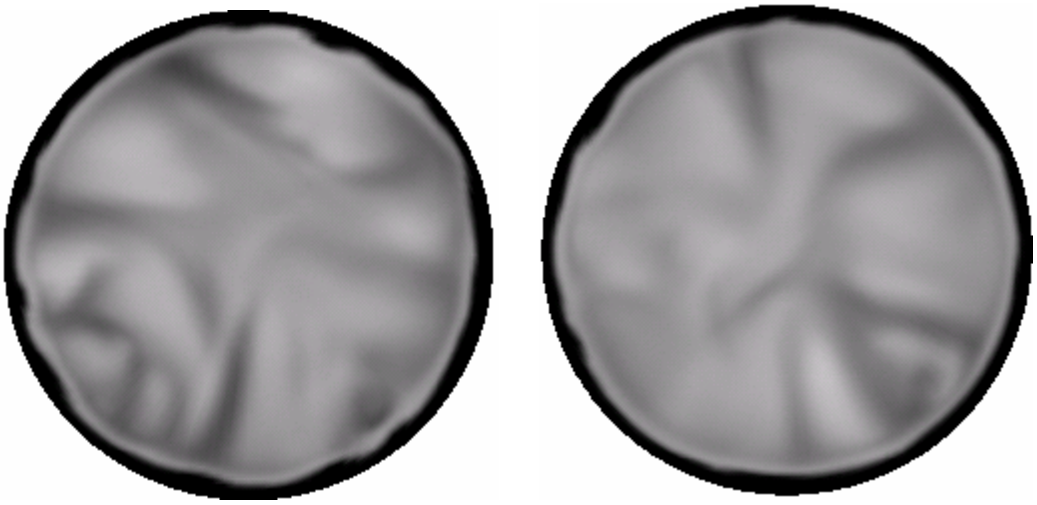

(a) (b)

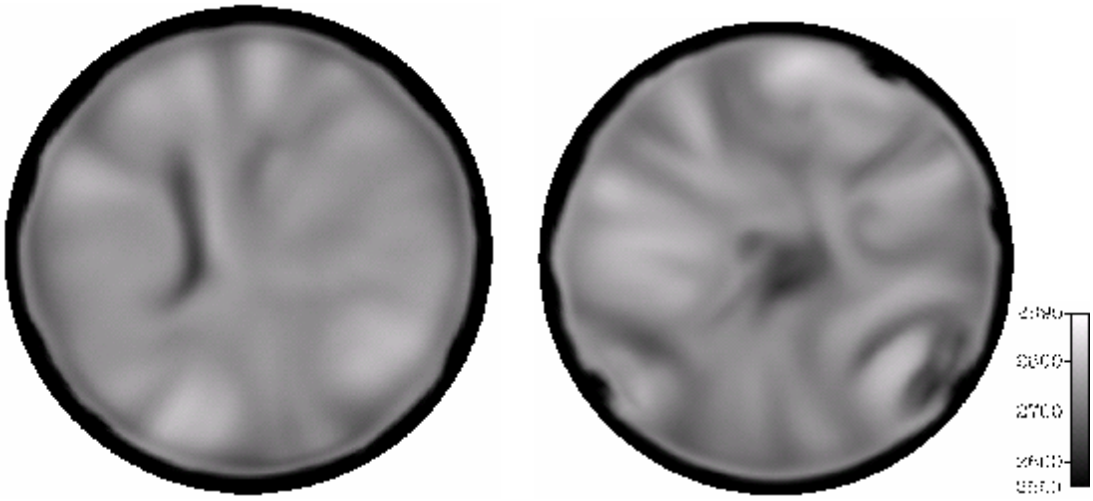

(c) (d)

Fig. 47. Temperature (° C) distribution across the melt free surface.

Dt = 0.5 s, sequence: left-right, top-down

The calculated free surface temperature averaged for the pyrometer central sighting spot (T_{ev}) was 2768°C, i.e. 160°C above the experimentally obtained value.

Therefore, a 3D flow calculation for regime #1 in both MC5 and MC4 provided a possibility of verifying physicomathematical models using the melt free surface structure – a high-quality flow characteristic.

At the next stage of investigations it would be of interest to reduce the size of computational cells in 3D geometry for the sake of a more complete direct modeling of a turbulent flow and reliable overcoming the Kolmogorov scale of turbulence.

Two-dimensional calculations, which are less reliable for studies of the space-time structure of a flow, though yield satisfactory results concerning temperature, heat fluxes and crust thickness, is planned to complement with the coordinated calculation of the electromagnetic problem. This will automatically link the Lorentz forces distribution and the volume heat sources to the evolving temperature field and the melt velocity, thus significantly raising the degree of the problem self-consistency. This may help overcome difficulties associated with calculating regimes ##3, 4 of MC5: the crust that appeared above the melt had not been taken into account in the electromagnetic problem, the results of which were used as external in the present paper.

Conclusions

- The MC4 and MC5 data were used for verifying models and software tools for 2D and 3D modeling of molten corium in the cold crucible.
- The type of boundary conditions for the cold walls and the corium-conjugated specimen surface has been identified.
- The possibility of direct modeling of turbulent flow using the complete system of Navier-Stokes equations has been demonstrated. This approach ensured satisfactory calculations of heat fluxes to the melt-confining surfaces, crust thickness on the bottom calorimeter in MC4 and on the specimen surface in MC5, temperature distribution in the specimen, and structure of the melt free surface. Some cases demonstrated satisfactory agreement between the calculated and experimental temperatures for the melt free surface center.
- The specimen temperature has been found to fluctuate in the specimen/corium system in the quasistationary state in MC5.
- Efficiency of the k-ω turbulence model for 2D calculations of heat fluxes, crust thickness and temperature in the melt surface center under the MC4 conditions has been demonstrated.

References

1. Loytsiansky L.G. Liquid and gas mechanics. Moscow, Nauka Publishers. 1973. 847 p. (Russ.)
2. Investigation of corium melt interaction with NPP reactor vessel steel (METCOR). Free convection in the molten pool. Test MC4/2000. Intermediate report. Project #833-99.
3. Investigation of corium melt interaction with NPP reactor vessel steel (METCOR). Phase №2. Progress report. 01/01/03 – 31/03/03. Investigation of Corium Melt Interaction with Reactor Vessel Steel in neutral above-melt atmosphere. Test MC5/03.
4. Gebhart B., Heat Transfer, 2nd ed., McGraw, N. Y., 1970.
5. Handbook of Turbulence. Fundamentals and Applications. Ed. by W. Frost, T. Moulden.. Moscow, Mir Publishers. 1980. 527 p. (Russ. translation)
6. V.Bojarevics, K. Pericleous. “Modelling Induction Melting Energy Savings” International Scientific Colloquium. Modelling for Saving Resources. Riga. May 17-18. 2001. pp. 11-16.
7. D.C. Wilcox. Turbulence modelling for CFD, 2nd ed., DCW Industries, California (1998).
8. Patankar S. Numerical Heat Transfer and Fluid Flow. Moscow. Energoatomizdat. 1984. 152 p.
9. Stedman S.J., Evans J.R.G., Woodthorpe J. 1990. Rheology of composite ceramic injection moulding suspensions, Journal of Material Science, 25, pp. 1833-1841.
10. Rasplav Final Report. Behavior of the corium melt pool in LWR vessel lower head with external cooling. July, 2000.
11. Vesiroglu T.N. Correlation of Thermal Contact Conductance Experimental Results. Prog. Astron. Aero., vol. 20, Academic Press, New York, 1967.
12. Thomas T.F., Probert S.D. Thermal Resistances of Some Multi-Layer Contacts Under Static Loads. / Int. J Heat and Mass Transfer, vol.9, 1966, pp. 739-754.
13. M. Hortmann, M. Peric, G. Scheuerer. Finite volume multigrid prediction of laminar natural convection: bench-mark solutions. Int. J. Numer. Methods Fluids. 11, 1990, p. 189-207.

Appendix 1

MC4 computations with the temperature boundary condition of the first kind

Additional thermal hydraulic calculations of the molten pool in MC4 are presented in this Appendix. They have been performed using simplified temperature boundary conditions. Here, adequacy of the boundary conditions used in the main part of the Report is demonstrated. The considered versions are given below.

1. The melt/crucible boundary is isothermal and impermeable. $T=T_{Liq}$, condition (23) is set for the bottom calorimeter surface at α=150 W/(m^2·K).

   Condition designation: **Liq/(23)**.

2. An isothermal wall condition $T=T_{Liq}$. is set for the melt/crucible and melt/bottom calorimeter boundaries.

   Condition designation: **Liq/Liq**.

3. An isothermal wall condition $T=T_{Sol}$ is set for the melt/crucible boundary and condition (23) is set for the bottom calorimeter surface at α=150 W/(m^2·K).

   Condition designation: **Sol/(23)**.

4. An isothermal wall condition $T=T_{Sol}$ is set for the melt/bottom calorimeter boundary.

   Condition designation: **Sol/Sol**.

Fig. P1-1 shows the distribution of temperature under the Liq/(23) conditions. Significant distortion of the lower crust shape is seen, and its thickness is underestimated in comparison with the experimental value. Under the Liq/Liq conditions, crust thickness is zero.

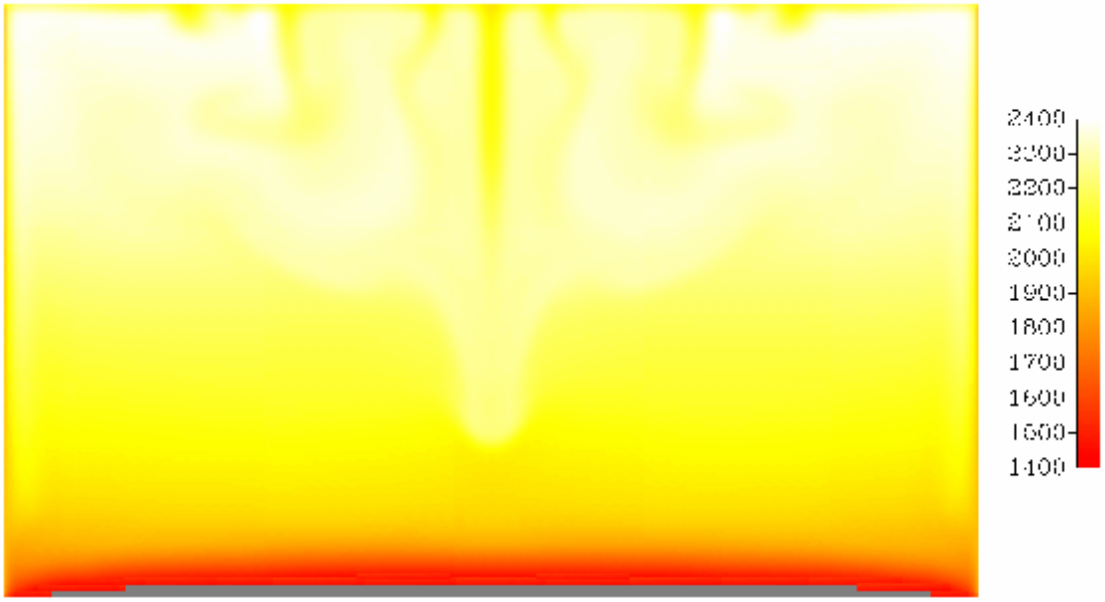

Fig. P1-1. Temperature (°C) distribution. Regime #1, MC4, Liq/(23) conditions

Tabs P1-1÷P1-4 summarize the results of calculations using the Liq/(23) and Liq/Liq conditions for regimes ##1÷4 in MC4. It follows from them that satisfactory results were obtained for the melt surface center, excluding regime #2.

Calculations were satisfactory for heat fluxes from the free surface to the melt and crucible for all four regimes.

Heat flux to the bottom calorimeter was calculated with a significant error, and crust thickness calculations were also unsatisfactory.

Table P1-1. Regime # 1.

Parameter	Test	Calculated **Liq/(23)** α=150	Calculated **Liq/Liq** α=150
Power of radiation from the melt surface, W	5300	5935 **12%**	5995 **13 %**
Temperature of the melt surface central spot	2025, C	2064, C **(41 K) 2%**	2073, C **(68 K) 3.3 %**
Crust thickness on the bottom calorimeter, mm	5.5	1.1 **80%**	0 **100%**
Power from the melt to:			
- crucible, W	10200	8717 **14.5 %**	10070 **13%**
- calorimeter central section, W	150	276 **84 %**	67 **55 %**
- calorimeter middle section, W	280	545 **95%**	99 **65 %**
- calorimeter extreme section, W	-	874	114

Table P1-2. Regime # 2.

Parameter	Test	Calculated **Liq/(23)** α=150	Calculated **Liq/Liq** α=150
Power of radiation from the melt surface, W	7000	9440 **35 %**	9512 **36 %**
Temperature of the melt surface central spot	2180, C	2360, C **(180 K) 8.2 %**	2359, C **(179 K) 8.2 %**
Crust thickness on the bottom calorimeter, mm	4.5	**0.9**	0 **100 %**
Power from the melt to:			
- crucible, W	21460	18911 **12 %**	20264 **5.6 %**
- calorimeter central section, W	160	291 **82 %**	81 **50 %**
- calorimeter middle section, W	320	590 **84 %**	137 **27 %**
- calorimeter extreme section, W	-	955	193

Table P1-3. Regime # 3.

Parameter	Test	Calculated **Liq/(23)** α=150	Calculated **Liq/Liq** α=150
Power of radiation from the melt surface, W	7400	7422 **0.3%**	7447 **0.6%**
Temperature of the melt surface central spot	2220, C	2220, C **(0 K) 0%**	2208, C **(-12 K) 0.5%**
Crust thickness on the bottom calorimeter, mm	14	**0.5**	0 **100 %**
Power from the melt to:			
- crucible, W	24080	23431 **2.6 %**	24806 **3 %**
- calorimeter central section, W	100	284 **186%**	64 **36%**
- calorimeter middle section, W	230	585 **154 %**	132 **43 %**
- calorimeter extreme section, W	-	945	193

Table P1-4. Regime # 4.

Parameter	Test	Calculated **Liq/(23)** α=150	Calculated **Liq/Liq** α=150
Power of radiation from the melt surface, W	5970	6533 **9.4 %**	6575 **10 %**
Temperature of the melt surface central spot	2090, C	2125, C **(35 K) 1.6 %**	2139, C **(49 K) 2.3 %**
Crust thickness on the bottom calorimeter, mm	14	1.2 **91 %**	0 **100 %**
Power from the melt to:			
- crucible, W	19190	17274	18591

		10 %	**3.1 %**
- calorimeter central section, W	95	273 **187 %**	62 **35 %**
- calorimeter middle section, W	-	560	134
- calorimeter extreme section, W	-	912	167

Fig. P1-2 shows temperature distribution under the Sol/(23) condition. It may be seen that the crust above the calorimeter center is calculated much better than under the Liq/(23) condition. However, there is still a significant error concerning the bottom crust shape at the calorimeter edge. Under the Sol/Sol conditions, the calculated crust thickness is zero.

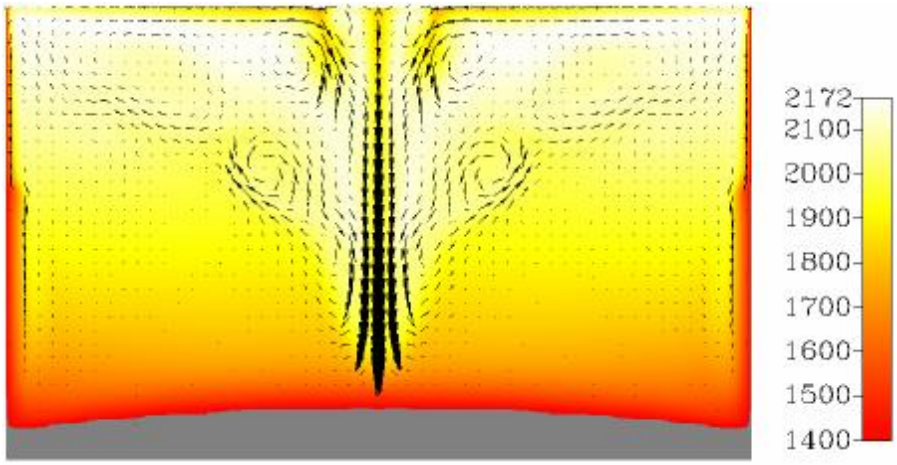

Fig. P1-2. Temperature (°C) distribution. Regime #1, MC4, Sol/(23) conditions

Tabs P1-5÷P1-8 summarize the results of calculations using the Sol/(23) and Sol/Sol conditions for regimes ##1÷4 in MC4. A comparison with the previous conditions Liq/(23) and Liq/Liq shows an increased error of calculating the melt surface center temperature, and a higher accuracy of calculations of crust thickness above the calorimeter center.

A comparison of the results obtained using the Sol/(23) and Sol/Sol boundary conditions with the results obtained under conditions (23) at all solid boundaries (Tab. 10) yields a conclusion that a transition to the Sol/(23) and Sol/Sol boundary conditions has increased the error of calculations of the melt surface center temperature and crust thickness.

It may be seen from Tabs. p1-5÷P1-8 that the Sol/(23) and Sol/Sol conditions provide satisfactory results of calculating heat fluxes from the melt free surface and those to the crucible.

For molten pools with small depths (regimes ##1, 2), condition Sol/(23) ensures high precision (error below 13%) of calculating heat fluxes to the bottom calorimeter sections. For deeper molten pools (regimes ##3, 4), however, the calculations of heat fluxes to the bottom calorimeter sections should better employ the Sol/Sol condition.

Table P1-5. Regime # 1.

Parameter	Test	Calculated **Solid/(23)** α=150	Calculated **Solid-Solid** α=150
Power of radiation from the melt surface, W	5300	4233 **20 %**	4283 **19 %**
Temperature of the melt surface central spot	2025, C	1883, C **(-142 K) 7 %**	1900 **(-125 K) 6 %**
Crust thickness on the bottom calorimeter, mm	5.5	4.8 **12 %**	0 **100 %**
Power from the melt to:			
- crucible, W	10200	11137 **9 %**	11503 **13 %**
- calorimeter central section, W	150	157 **5 %**	90 **40 %**
- calorimeter middle section, W	280	316 **13 %**	196 **30 %**
- calorimeter extreme section, W	-	505	260

Table P1-6. Regime # 2.

Parameter	Test	Calculated **Solid/(23)** α=150	Calculated **Solid-Solid** α=150
Power of radiation from the melt surface, W	7000	6771 **3 %**	6778 **3 %**
Temperature of the melt surface central spot	2180, C	2106, C **(-74 K) 3.4 %**	2145, C **(-35 K) 1.6 %**
Crust thickness on the bottom calorimeter, mm	4.5	3.7 **18 %**	0 **100 %**
Power from the melt to:			
- crucible, W	21460	22355 **4.2 %**	22692 **5.7 %**
- calorimeter central section, W	160	170 **6.2 %**	109 **32 %**
- calorimeter middle section, W	320	346 **8.1 %**	240 **25 %**
- calorimeter extreme section, W	-	552	383

Table P1-7. Regime # 3.

Parameter	Test	Calculated **Solid/(23)** α=150	Calculated **Solid-Solid** α=150
Power of radiation from the melt surface, W	7400	5255 **29%**	5307 **28%**
Temperature of the melt surface central spot	2220, C	2014, C **(-206 K) 9.3%**	2016, C **(-184 K) 8.2%**
Crust thickness on the bottom calorimeter, mm	14	4.4 **68 %**	0 **100 %**
Power from the melt to:			

- crucible, W	24080	26437 **10 %**	26636 **10 %**
- calorimeter central section, W	100	160 **60%**	106 **6%**
- calorimeter middle section, W	230	329 **43 %**	260 **13 %**
- calorimeter extreme section, W	-	526	380

Table P1-8. Regime # 4.

Parameter	Test	Calculated **Solid/(23)** α=150	Calculated **Solid-Solid** α=150
Power of radiation from the melt surface, W	5970	4710 **21 %**	4721 **21 %**
Temperature of the melt surface central spot	2090, C	1947, C **(-143 K) 6.8 %**	1950, C **(-140 K) 6.7 %**
Crust thickness on the bottom calorimeter, mm	14	5.1 **64 %**	0 **100 %**
Power from the melt to:			
- crucible, W	19190	19736 **2.8 %**	20140 **5 %**
- calorimeter central section, W	95	138 **31 %**	97 **2 %**
- calorimeter middle section, W	-	278	230
- calorimeter extreme section, W	-	470	329

Basically, the results given in this Appendix and in Section 3.1 show optimality of using condition (23) with α=150 W/(m^2·K) for all solid boundaries of the melt in the main part of this investigation, as it yielded satisfactory results concerning both heat flux values and temperatures with a plausible shape of the crust on the bottom calorimeter for all regimes of MC4.

Appendix 2

Computations disregarding electromagnetic forces

A significant difference between structures of the free convective flows in MC4 and MC5 was explained in the present Report by the increase of electromagnetic forces at the transition from MC4 to MC5, Figs. 8, 9, 11, 12.

In order to identify the electromagnetic forces' role, they were disregarded in computations described in the present Appendix. Regimes #4 in MC4 and #1 in MC5 were considered. The neglect of electromagnetic forces in computations for MC4 has caused a hardly noticeable change of the calculated parameters, but it does not refer to MC5.

Fig. P2-1 shows temperature distribution during regime #1 in MC5 disregarding the Lorentz forces. A comparison with Fig. 34 shows that crust thickness on the bottom calorimeter has increased by an order of magnitude, while peak temperature in the melt – by 200°C. With such a crust thickness, no satisfactory result concerning temperature distribution in the specimen should be expected. Indeed, the neglect of electromagnetic forces has caused a drop of the temperature at the thermocouple TC02 location to 485°C, i.e. for about 500°C.

An explanation of such a fact may be that in MC4 and MC5 the electromagnetic forces vector is directed downwards, therefore the stronger the Lorentz forces are, the higher their importance for heat transport to the bottom crust is, i.e. their influence on the bottom crust thickness increases.

In MC4 the Lorentz forces were much weaker than in MC5 and likewise their influence on thermal regime of the molten pool bottom.

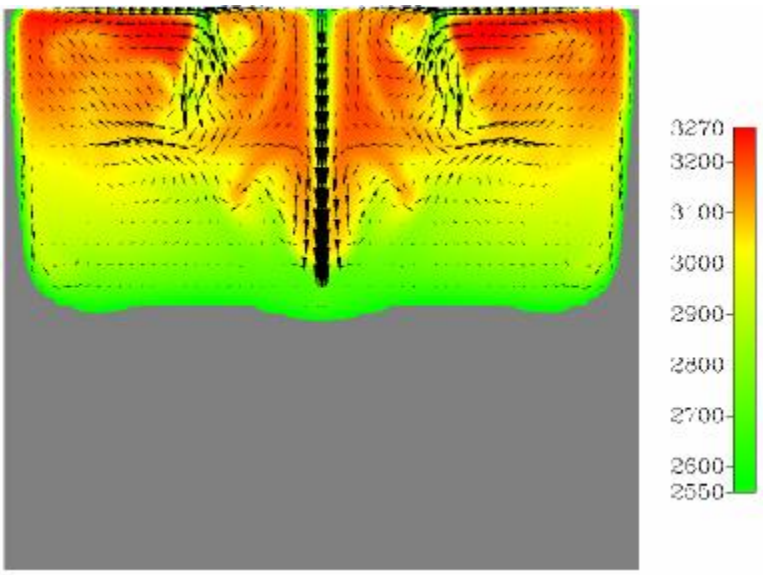

Fig. P 2-1. Temperature (°C) distribution. Regime #1, MC5, disregarding electromagnetic forces